Strain Rate Analysis in Bulge Test

by

Kamil Buğra Toga

A Thesis Submitted to the
Graduate School of Sciences and Engineering
in Partial Fulfillment of the Requirements for
the Degree of

Master of Science
in
Materials Science and Engineering

Koc University

January 2008

Koc University

Graduate School of Sciences and Engineering

This is to certify that I have examined this copy of a master's thesis by

Kamil Buğra Toga

and have found that it is complete and satisfactory in all respects,
and that any and all revisions required by the final
examining committee have been made.

Committee Members:

_____

Erdem Alaca, Ph. D. (Advisor)

_____

Alper Kiraz, Ph. D.

_____

Demircan Canadinç, Ph. D.

Date: January 25, 2008

ABSTRACT

A powerful mechanical characterization method applicable to sub-micron membranes is qualified to determine strain rate dependent yield behavior of free standing gold films. In this technique, the stress-strain behavior of gold is determined from the pressure-deflection behavior of a long rectangular diaphragm. Constant strain rate condition is derived from a readily available analytical model and implemented to the automation facility. A traditional silicon micromachining technique is performed to open 500 nm thick gold diaphragms. The significant considerations on sample preparation, experimental procedure and data acquisition are evaluated. Young's modulus is measured smaller than the bulk value which is verified by the literature and the crystallographic texture analysis. Residual stress and yield strain is found to be in agreement with finite element simulations. The yield stress of gold films differed considerably at different strain rates increasing at rapid measurements.

ÖZET

Önemli bir mekanik karakterizasyon tekniği olan şişirme deneyi, mikron-altı kalınlıktaki altın ince filmlerin sabit gerilim hızı koşullarındaki akma mukavemetini ölçmek için özelleştirildi. Altının baskı-gerilim davranışı ince uzun bir dikdörtgen diyaframın şişirme methodu ile ölçülen basınç-esneme davranışından elde edildi. Sabit gerilim hızı koşulu hali hazirda var olan bir analitik modelden türetildi ve deney düzeneğinin otomasyonuna dahil edildi. 500 nm kalınlıktaki diyaframlar yaygın olarak kullanılan Silikon mikro fabrikasyon tekniğiyle üretildi. Numune hazırlanması, deney düzeneğinin detayları, deneyel prosedür ve data alımı-işlenmesi etraflıca değerlendirildi. Elastik modül kalıp halindeki altın malzemenin elastik modülünden düşük bulundu; kristal yapı analizleri ve literatürdeki değerler mevcut durumu destekledi. Malzemenin akma mukavemetinin artan gerilim hızına bağlı olarak arttığı gözlemlendi.

ACKNOWLEDGEMENTS

I would like to express my gratitude to all those who gave me the possibility to complete this thesis. I am deeply indebted to my supervisor Professor Alaca from Koc University Istanbul whose help, stimulating suggestions and unlimited encouragement helped me in research. I would love to dedicate this work to such a great mentor like him who always trusted me as a worker, as a student and more significantly as a person. I am also greatful for the unlimited support of Professor Tayfun Akın and Orhan Akar of METUMEMS, Professor Demircan Canadinç from KU Department of Mechanical Engineering, and Professor Alper Kiraz form KU Physics Department. I will always remember the friendship and collobration in Alaca Group 2004-2008.

TABLE OF CONTENTS

LIST OF TABLES

LIST OF FIGURES

NOMENCLATURE

E	Young's modulus
υ	Poisson's ratio
σ	stress
σ_0	residual stress
σ_y	yield stress
σ_u	ultimate stress
ε	strain
ε_0	residual strain
a	half of membrane width
d	thickness of membrane
h, h_f	center deflection of membrane
h_s	substrate deflection
h_t	total measured deflection at the center of the membrane
h_0	initial deflection of the membrane
c	strain rate
t	time
C_1, C_3	polynomial constants for the analytical blister model
τ	dummy index for time
δ	dummy index for film deflection
α	constant of proportionality between pressure and substrate deflection

Chapter 1

INTRODUCTION

1.1. Overview

Nano and *micro* are prefixed with other terms specializing the general meaning of the original concept into the narrow boundaries of molecular and morphological scales of materials respectively. Nanotechnology refers to the engineering applications created by nano-sized devices and assembly of molecules. In order to explain a mechanism existing in nanoscale, scientists usually refer to the theory of statistical mechanics and simulations of molecular dynamics. Beyond nanoscale, in the smaller extreme, physical mechanisms are explained by quantum mechanics; meanwhile, in the larger extreme, *i.e.* the microscale and beyond, the applicable theory stands as continuum mechanics. The theme of this work is analysis and development of an experimental research method applicable in microscale.

Microtechnology requires materials to be tailored into small dimensions such that a microsystem is usually a composition of various thin film layers. Confined into a bounded space, materials are influenced by surface and interfacial effects [1]. Therefore, Microsystems are expected to show different physical properties than their bulk counterparts. This is one of the motivations for scientists to investigate the physical mechanisms occurring at small scale.

Mechanical properties and reliability of thin films have become significant research fields as Micro Electro Mechanical Systems (MEMS) and microelectronics have extended their technological importance [2]. The mechanics of small structures cannot be directly studied using the bulk properties [3]. Microstructural features of

polycrystalline films such as grain size or crystallographic texture cannot be similar to those in the bulk, because the grain growth is limited by thickness. Due to the same reason, dislocation and grain boundary sliding mechanisms may alter as size scale gets smaller. As a result of this extreme, the plastic behavior of a polycrystalline material is expected to be different in the form of a thin film [3].

Another motivation to study the physics of thin films emanates from the need to secure the mechanical reliability of small devices [4]. Thin films may deform or fail as they sustain extensive amounts of loads. Materials can be critically stressed due to their structural functions. Microfabrication processes can also induce strains within materials. Since microfabrication processes takes place in extreme thermodynamic conditions, materials can experience spatial changes before they reach to equilibrium. Among these thermodynamic effects, thermal expansion mechanism plays a critical role within a film fabricated on a substrate. Having different coefficients of thermal expansion, each unique fabrication layers stimulates large residual strains if they are confined on each other at elevated temperatures. This physical mechanism can cause material deformation, malfunctioning or even failure in ambient process conditions.

All the circumstances encountered above have obliged thin film characterization. Therefore, various mechanical characterization methods applicable to thin films have been developed. One can classify these methods in two main categories. The first category of techniques requires rather detailed sample preparation. Tensile test, bending test and bulge test are related to such a practical scheme. The latter category includes testing of thin films on substrates as in the cases of indentation test and substrate curvature technique. In this study, bulge test is facilitated to characterize free standing gold films with submicron-thickness.

1.2. Mechanical Characterization Methods in Microscale

Mechanical characterization in microscale [5,6] is a rather difficult task for several reasons. Sample preparation requires elaborate micromachining efforts. Once

fabricated, the samples should be handled gently and attached carefully to the test set-up. As size scale decreases, higher resolution actuation and higher sensitivity data acquisition becomes indispensable. In this section, utilities and limitations of widely used experimental methods like substrate curvature test, indentation test, tensile test, bulge test and bending test will be presented.

1.2.1. Microindentation

Microindentation [7] method is a microscale analogous of the well known hardness test. This method was adapted to small scale specimens after depth sensing indentation devices [8] were invented. In a typical indentation test, a hard probe is penetrated into the film and the depth of penetration is measured as a function of the applied pressure. The indentation tip can be either spherical, conical or pyramidical.

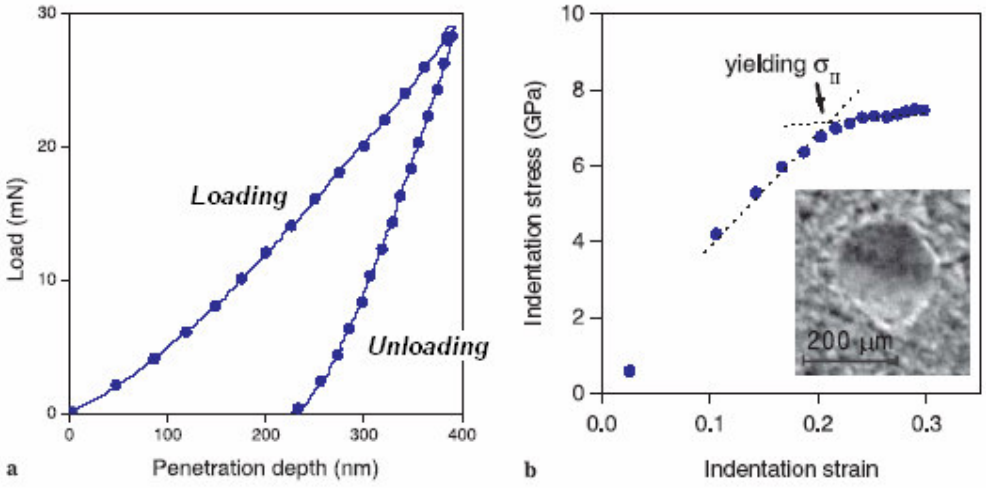

Figure 1.1: (a) Load vs. Penetration Depth curve for Cr, measured with 5-µm-radius indenter. (b) Corresponding indentation Stress vs. Strain curve [9]

A typical load-penetration curve for indentation test is shown in figure 1.1. In principle, from indentation analysis, one can determine the modulus and the hardness of materials and estimate yield strength, σ_y and ultimate strength, σ_u values of a film of interest. There are important considerations to get accurate results in an indentation experiment. Ductile materials, especially metals, can pile up as the indenter penetrates into the sample. On the other hand, if the material is brittle, cracks might initiate due to applied compressive load. In addition, polycrystalline grains may sink through the film. An experimenter should interpret these mechanisms to ensure the accuracy of the final results.

1.2.2. Substrate Curvature Technique

Many mechanical characterization methods applicable to microscale thin films are inspired from the experiments originally designed for bulk materials. Among the techniques that have been mentioned so far, substrate curvature is the only one that is merely used for microfabricated samples. It is a utility to determine the biaxial residual stress in a thin film. In the analytical model, residual stress is a function of a measured parameter, radius of curvature and design parameters like film thickness and substrate stiffness. The principle of this technique relies on the fact that stress in a thin film is inversely proportional to the radius of curvature of the substrate it lays on [4]. This is valid as long as the film thickness is much smaller than the substrate thickness [10]. On the other hand, substrate curvature technique is not capable to determine other mechanical properties like Young's modulus, yield stress, and Poisson's ratio.

1.2.3. Microtensile Test

Tensile test is the most widely used mechanical test in bulk material analyses. A Complete set of mechanical properties can be measured using this method. The micro-specimens are usually designed in dog bone geometry and uniaxially loaded till failure.

Stress-strain diagrams are directly plotted using measured parameters load and extension. The bulk method can be applied to microfabricated samples as well. A test sample with dog-bone geometry is micromachined inside a silicon frame. Readily gripped in a rigid structure, the sample can be securely attached to the actuator. Each test can be ran at desired strain rates [11], at desired temperatures [12] allowing *in-situ* electron microscope analysis of samples [13].

1.2.4. Microbending Test

Bending test *a.k.a.* beam deflection test can be performed on a microfabricated cantilever. A micro-cantilever is a well defined rectangle fixed at one end and bound on a substrate. Fabrication errors tend to occur as design of cantilevers get smaller. Deviations in the designed geometry might create uncertainty in experimental results. In order to verify the experimental results in small scale, one should repeat a bending test on multiple samples. In a typical microbending test, the cantilever is tilted by an indenter and the tip deflection is measured. If the material of interest is soft, the indenter penetration into the sample should be subtracted from the total displacement. Like substrate curvature method, microbending technique can also determine the residual stress in the sample. In residual stress analysis, a film of interest is deposited on a thicker cantilever (*i.e.* substrate) and residual stress is measured referring the tip deflection data. Yield behavior of the materials is also observable via using a similar experimental approach.

1.2.5. Bulge Test

Bulge test studies center deflection of a membrane resulting from applied fluid pressure. This method was first studied by J.W. Beams in 1959 [14] and fully adapted to microfabricated films by Vlassak and Nix in 1992 [15]. From pressure-deflection data, one can extract many mechanical properties like Young's modulus, Poisson's ratio,

yield stress, ultimate stress and residual stress of thin films. Following chapters will focus on the specialization of the method into a strain rate controlling facility.

1.2.6. Comparison of Micromechanical Testing Techniques

There have been examples of review studies [5, 6] and experimental analyses [16-19] comparing the capacities and limitations of mechanical characterization methods. As indicated above, some methods are relatively cumbersome in terms of sample preparation and experimental practice. Likewise, some methods are advantageous over the others in investigation of specific properties. Indentation method is the single method determining the hardness in small scale, but Young's modulus and Poisson's ratio cannot be directly measured with an indenter. Since Poisson's ratio is a geometry dependent property in analytical bending models, one can easily measure it performing bulge test on diaphragms of different geometry [20, 21]. Besides, bulge test and tensile test are in the solitude position to directly measure the complete stress-strain behavior of small samples; whereas, the indentation method misses such a utility.

All methods except indentation are applied on large volumes of materials allowing one to extract average material properties. A single measurement of an indenter can merely determine local properties of a large sample. Therefore, one should take measurements from multiple points in order to attain a reliable mean result from an indentation analysis.

Chapter 2

BULGE TEST

2.1. Overview

Bulge Test, *a.k.a.* Blister Test, is a versatile characterization method capable to determine a complete set of mechanical properties of thin films in various thermodynamic conditions. The first effort to adapt the technique to micro scale focused on determining residual stress in thin evaporated metal films on silicon nitride (SiN_x) wafers [22]. Then, the method was exploited to measure elastic properties of thin films like Poisson's ratio and modulus of elasticity [15]. Bulge test has proved to be capable to perform more complicated analyses like dynamic mechanical tests [23, 24], fatigue test [25], transient creep analysis [26], high temperature creep analysis [27], high temperature plasticity analysis [28] and viscoelasticity analysis [29]. The method is shown to be applicable not only to metals [23, 26-32] but also to ceramics [33-35] and to polymers [36-38]. So far, the literature has been missing a published study exploiting the bulge test in a strain rate dependent material property analysis. This study aims to reveal the method's practicality to load the samples at specific strain rates and thus create a link between the strain rate dependent mechanical properties and microstructure of the materials.

2.2. Theory

A rectangular membrane with 10:1 aspect ratio is pressurized and the deflection h at the center of the membrane varies as a function of the pressure. The deflection is not

only dependent on the applied pressure but it is also a function of sample geometry and isotropic material parameters. In the elastic regime, for a linear elastic membrane, the relationship between pressure, *P*, and deflection, *h*, is given in a polynomial form [15] as

$$P = C_1 \frac{\sigma_0 d}{a^2} h + C_3 \frac{Ed}{(1-\nu)a^4} h^3 \tag{2.1}$$

where σ_0 is in plane biaxial residual stress, *E* Young's modulus, *v* Poisson's ratio, *d* membrane thickness and *a* half of the membrane width. This model is a good approximation for membranes of various geometries. C_1 is a geometry dependent constant and C_3 depends on both the geometry of the membrane and the Poisson's ratio of the material. For rectangular membranes with high aspect ratios, the above equation takes the following form:

$$P = 2\frac{\sigma_0 d}{a^2} h + \frac{4}{3}\frac{Ed}{(1-\nu^2)a^4} h^3 \tag{2.2}$$

This representation is valid as long as the membrane is loaded in the elastic regime. The geometry of the deflected membrane can be considered as a sliced cylinder, if the aspect ratio of the rectangle is large. In a cylinder-like geometry, stress gradients are negligible along the width of the loaded membrane.

Whether the membrane is plastically or elastically loaded, the stress, σ and the strain, ε across the width of the sample are represented by the following equations:

$$\sigma = P\frac{(a^2 + h^2)}{2hd} \tag{2.3a}$$

$$\varepsilon = \varepsilon_0 + \frac{\left(a^2 + h^2\right)}{2ah}\arcsin\left(\frac{2ah}{\left(a^2 + h^2\right)}\right) - 1 \qquad (2.3b)$$

where ε_0 is the residual plane strain. Since h is much smaller than a, equations 2.3 can be rewritten as

$$\sigma = \frac{Pa^2}{2hd} \qquad (2.4a)$$

$$\varepsilon = \varepsilon_0 + \frac{2h^2}{3a^2} \qquad (2.4b)$$

This reduction is valid for strains less than 1%. For highly deformable materials, one should use the former version.

Taking the first derivative of strain with respect to time, t, strain rate c can be derived:

$$c = \frac{4}{3a^2} h \frac{\partial h}{\partial t} \qquad (2.5)$$

Replacing the dummy variables, δ and τ with h and t respectively; one can solve the new differential equation as follows

$$\int_{h_0}^{h} \delta d\delta = \int_{0}^{t} c \frac{3a^2}{4} d\tau$$

$$h^2 = h_0^2 + c\frac{3a^2}{2}t \qquad (2.6)$$

For a flat membrane exposed to gauge pressure, the initial deflection, h_0, in equation 2.6 is negligible. Hence, the center displacement of a rectangular membrane at constant strain rate c exhibits square root time dependence as in equation 2.7:

$$h = \frac{a\sqrt{3c}}{\sqrt{2}} t^{1/2} \tag{2.7}$$

The final result given in equation 2.7 will be revisited in chapter 4 while we discuss the effect of substrate deflection on measurements.

2.3. Test Set-up

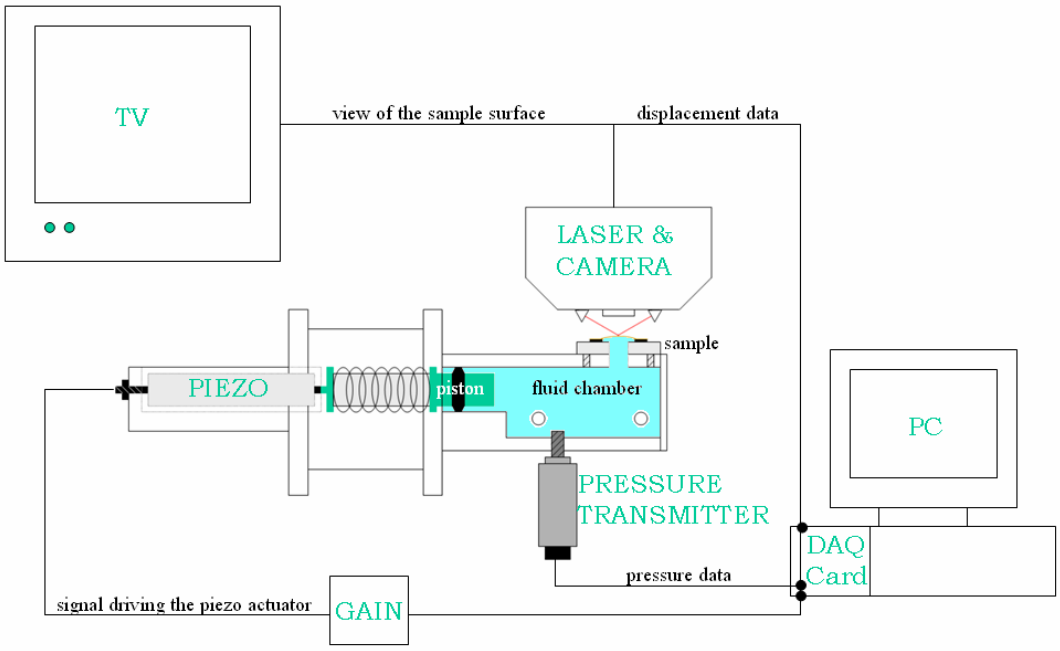

Figure 2.1: 2D Schematic of Bulge Test

Figure 2.1 provides the 2D schematic of the bulge test experiment. The set-up is basically designed to take two important streams of data, variable fluid pressure in the chamber and accompanying center deflection of the symmetric membrane. There are two sensors serving these tasks: The piezoresistive (pressure) transmitter is pressure sensing device and the laser sensor is position sensing device measuring vertical distance between a point on the sample surface and the sensor.

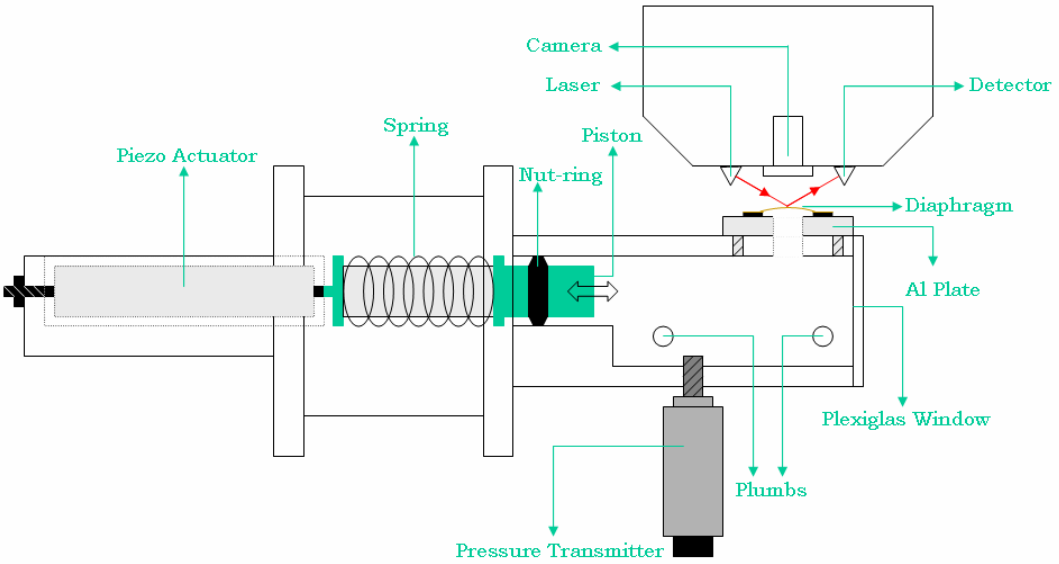

Figure 2.2: The Main Body

The main body of the experimental set-up is depicted in figure 2.2. During tests, the diaphragm is loaded by push of the piston which is driven by the piezoelectric actuator. The actuation is utilized by the analog signal coming from a PC controlled data acquisition (DAQ) card (Refer section 4.1.1 for DAQ specifications). The motion of the actuator is transferred to a piston by a coupling spring system. The cylindrical piston can compress or decompress volume of the fluid enclosed in an isolated chamber. The chamber needs to be perfectly enclosed in order to attain sufficiently high pressure; and accordingly measures the complete mechanical behavior.

Isolation of the fluid chamber is a significant issue influencing amount of maximum stress applicable to a diaphragm. The chamber has five open sites connecting various members, *e.g.* pressure sensor, plumbs, piston *etc.* which make the way out for pressurized liquid. Three of the five sites, the pressure sensor-chamber interface and two plumbs, are sealable by Teflon© membranes in order to avoid fluid leakage. The Teflon© isolator is a white flexible film tightly stretchable around screw shafts. The shafts should be wrapped in counterclockwise direction, the direction of screw loosening; otherwise, Teflon can crumple on itself and malfunction.

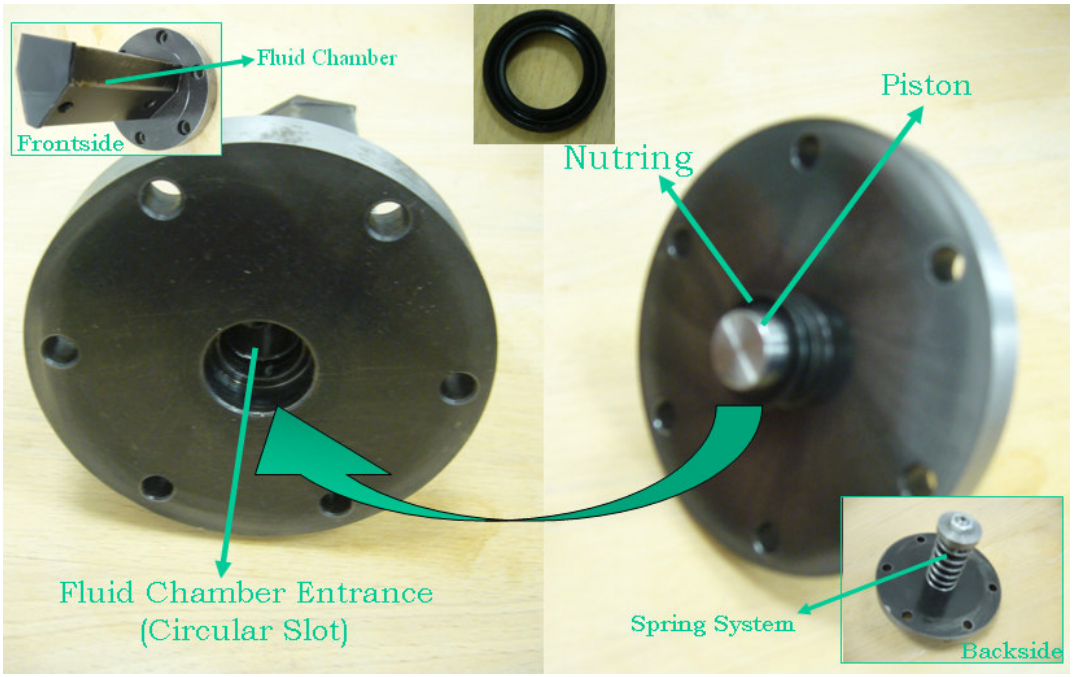

Figure 2.3: Dissembled Fluid Chamber-Piston System

The fluid chamber, the piston, the spring system and the nut-ring are dissembled and photographed as shown in figure 2.3. The cylindrical piston is sealed by a rubber nut-ring (u-ring) passing through a circular slot with 40 mm diameter. The nut-ring has a 15 mm inner perimeter strongly covering the outer perimeter of the piston. In the mean time, the outer perimeter is in tight contact with the circular slot. The piston can easily

slide through the nut-ring, while the pressurized fluid is kept in the chamber. The nut-ring is a commercially available product manufactured by a Turkish rubber company KASTAŞ. It is marketed as U-Ring 22-15-4.

The final opening of the chamber is a circular window showing the through view of the enclosed fluid. Initially, there was an effort to use regular glass to close this opening, but the brittle material failed to isolate the chamber perfectly. The window is now made of a commercial Plexiglas© that is available in local markets. It is glued on the steel frame by a strong commercial adhesive. Looking through the window, the experimenter can check if there is any bubble remaining in the enclosed space. The existence of bubbles would dismiss an experiment since the compression of the piston is absorbed by air domains instead of the hydraulic fluid. The ventilation of bubbles and other details about sample clamping will be discussed in section 3.2.3.

2.4. Sensors and Actuator

2.4.1. Laser and Specular Reflective Sensor

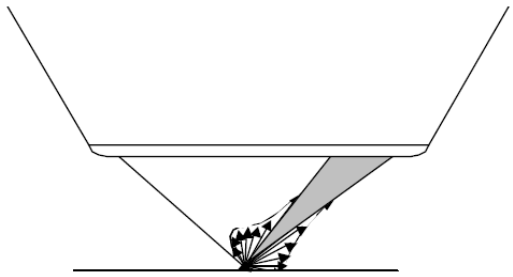

Figure 2.4: The Specular Reflection Sensor [39]

The deflection of the membrane at the center of the diaphragm is measured by a specular reflective sensor. As shown in figure 2.4, the specular reflection can pick up a major part of the reflected beam. The device is intended for measuring surfaces ranging from perfect mirrors to semi-specular surfaces such as aluminum, stainless steel and

other reflective materials. The beam used for such a mechanism is a red laser. The laser has a 10 μm beam spot for small features. Resolution in the sub micron range is achievable in microscale applications.

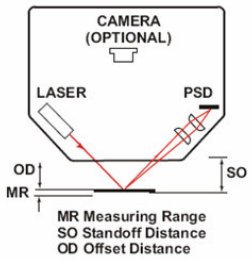

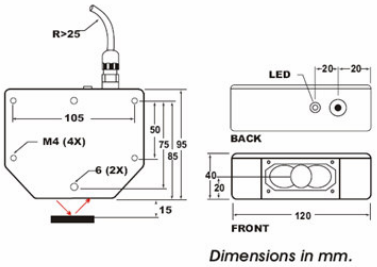

Technical Specification

Model Number		Measurement Range (MR)	Stand Off (SO)	Offset Distance (OD)	Resolution (Worst Case) Note 1	Resolution (Typical) Note 2	Linearity Note 3	Triangulation Angle at SO	Spot Size at SO
SLS 7001/15	mm	1	15	14.5	0.00025	0.000025	0.0005	86 deg.	0.010-0.020
	in	0.04	0.59	0.57	0.00001	0.000001	0.00002		0.0004-0.0008

Figure 2.5: The Sensor Head and Device Specifications [39]

The basic SLS7000 sensor consists of two parts: the sensor head (figure 2.5) and the controller. A 3 m long cable connects the controller to the sensor head. A red LED on the sensor head indicates if the power is on. There are two other LED's on the top surface of the controller indicating valid data in the measurement range (green LED) or invalid data/out of range (yellow LED) condition. The analog output is generated in the form of electrical current. 1 mA change in the output signal corresponds to a 0.0512 mm change in the absolute distance between the target and the sensor. If the target gets closer, the signal increases; or vice versa. The analog output is converted to voltage by a simple circuit (figure 2.6). In the connection circuit, 459 Ω load resistor is used which generates 9.18 V = 20 mA x 459 Ω signal difference for 1 mm = 20 mA x 0.0512 mm/mA net translation. This estimation is verified when the device is calibrated for measurements of 100 μm net displacement resulting 0.891 Volt difference in output signal.

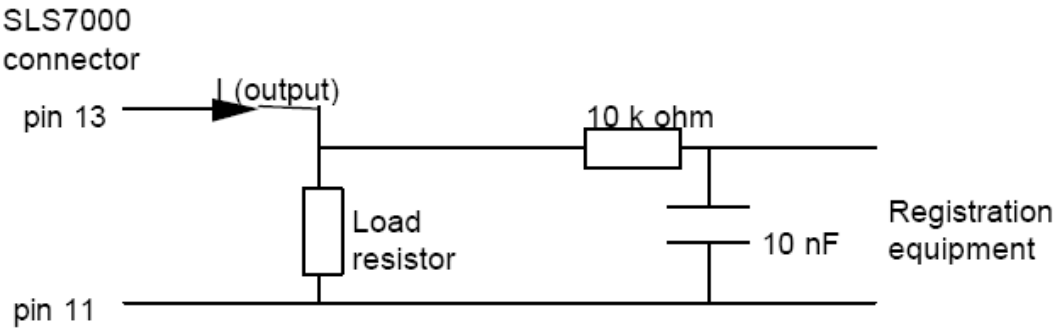

Figure 2.6: The Connection Circuit

2.4.2. Pressure Sensor

In comparison to the displacement sensor, the pressure sensor is a less complicated setting. The device is a commercial product having a wide range of applications at *e.g.* refrigeration, hydraulic controls, air compressors, ink jet printers, vacuum pumps *etc*. It is a KELLER OEM piezoresistive transmitter generating output in the range of 4-20 mA. A 248 Ω resistor is serially connected to the device converting the output in the range of 0.992 to 4.960 Volt. Approximately 1 Volt signal corresponds to the atmospheric pressure, while ~5 Volt is the maximum measurable limit indicating 1 bar inlet pressure. The output range is scaled by 0.5% resolution. The input voltage can vary between 8 and 28 Volts which can be generated by an external power supply. The tip of the pressure sensor is a gas screw which is in contact with the fluid chamber.

2.4.3. Piezo Actuator

A piezoelectric material changes its dimensions due to the polarization in applied electric field. Such a mechanism is exploited to design high resolution sub micron positioning devices. In the test set-up, a high voltage piezoelectric actuator, PI E-507, facilitates the translational motion of the hydraulic piston. The device is a 16 cm long

slim cylinder located at the tip of a spring system. A 2 m cable connects the device to a high voltage amplifier. Input signal received from the DAQ card is 100 fold amplified capable to stimulate 1 mm elongation. The whole actuation mechanism has more than 0.1% resolution. As a result of such a fine resolution, the output signal can easily be controlled by a manual potentiometer as well.

Chapter 3

SAMPLE PREPARATION & EXPERIMENTAL PROCEDURE

3.1. Microfabrication of Thin Films

3.1.1. Silicon Wafer

A silicon wafer with a diameter of 4 inches and a thickness of 200±10 μm is used as the template of the microfabrication process. The single crystal silicon has a texture in <111> orientation and an electrical resistivity of 5 mili-ohm/cm. Before starting the process, the wafer goes respectively through "Piranha Cleaning" (a bath of Sulfuric Acid (H_2SO_4) + Hydrogen Peroxide (H_2O_2)) and "Oxide Etch" (buffered Hydrofluoric Acid (HF)) to get rid of the organic residue on the surface. At the end of each process, the wafer is rinsed with deionized (DI) water (for 5 cycles after "Piranha Cleaning" and for 3 cycles after "Oxide Etch") and dried with N_2. Finally, cleaned wafer is kept in a dehydration bake under 110°C N_2 atmosphere for 15 minutes where it becomes ready for metal deposition.

3.1.2. Metal Deposition

The silicon wafer is first covered with a layer of 20 nm chromium (Cr). Then, 500 nm thick gold (Au) is sputtered over the adhesive layer. The first photolithography process is applied on the Au layer which is referred as the front side of the wafer. Prior to the deposition of the photoresist (PR: S1828), Hexamethyldisilazane (HMDS) is laid on gold to avoid the strong interaction between the PR and the metal surface. Then, the

sample is “soft-baked” for 1 minute under 115˚C in order to solidify the PR layer. The wafer is aligned beneath the mask, and exposed to ultraviolet light to create the mask patterns. The developer is laid on the top layer to get rid off the PR that was not protected by the mask against UV.

At the end of the first lithography, the piece is rinsed with DI water twice, (first for 2½ minutes and second for 1 minute) and dried with N_2. O_2 plasma is applied for 3 minutes in order to ensure that there is no excessive PR leftover. The piece is “hard-baked” under 115˚C for 30 minutes, so the patterned PR becomes stronger. The PR is finally lifted off in acetone after 10 nm titanium layer is sputtered on top to create icons. Dehydration takes place in a 110˚C oven under N_2 atmosphere for 20 minutes. The top of the metals is covered with a protective layer and hardened via baking at 115˚C for 30 minutes.

3.1.3. Window Etching

The second photolithography takes place on the back side of the wafer. A procedure similar to the first lithography is applied. HMDS is laid on the silicon surface and covered with a new photoresist material (PR2: SPR220-7). After the piece is soft-baked for 30 minutes, it is aligned with the mask and subjected to UV. The developer is delivered in order to cast away PR2. The piece is rinsed with DI water twice (first for 2½ minutes and second for 1 minute), and then dried with N_2. O_2 plasma is applied and cleaned the undesired PR2 portions from the surface. The piece is baked again at 115˚C for 30 minutes in order to harden the remaining PR2 layer. Finally, Deep Reactive-Ion Etching (DRIE) is applied to create diaphragm windows in silicon wafer. During DRIE process, PR2-free areas are deeply dug by a strong acid.

The photoresists on the both sides of the final product are stripped with a strong solution (SVC-175); nevertheless, the metal side is covered with a protective photoresist layer. As the microfabrication process is over, the circular wafer is diced into square test chips by a sharp diamond tip. Each chip consists of three or more diaphragms as shown

in figure 3.1. Some diaphragms look empty due to the inability of design software to exhibit the small components at centimeter resolution.

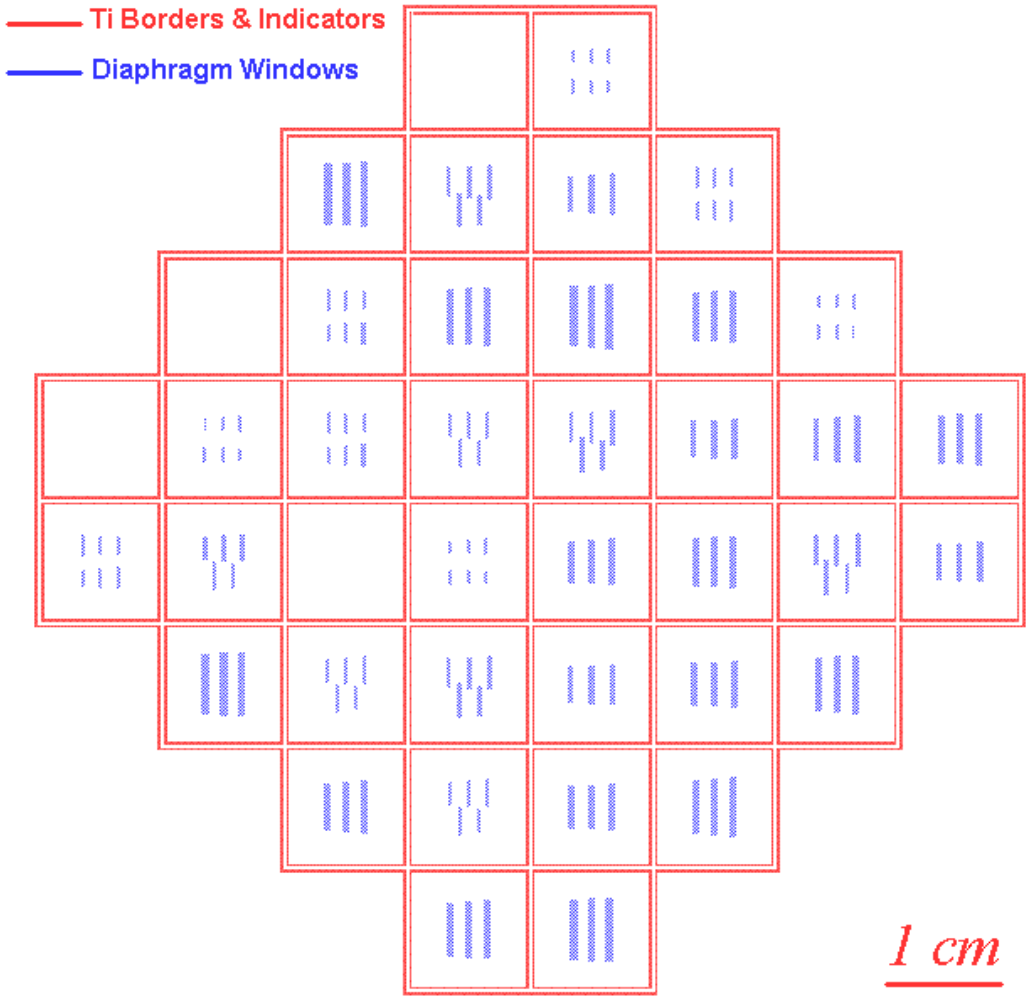

Figure 3.1: Lithography Mask

The microfabrication process flow is shown in figure 3.2.

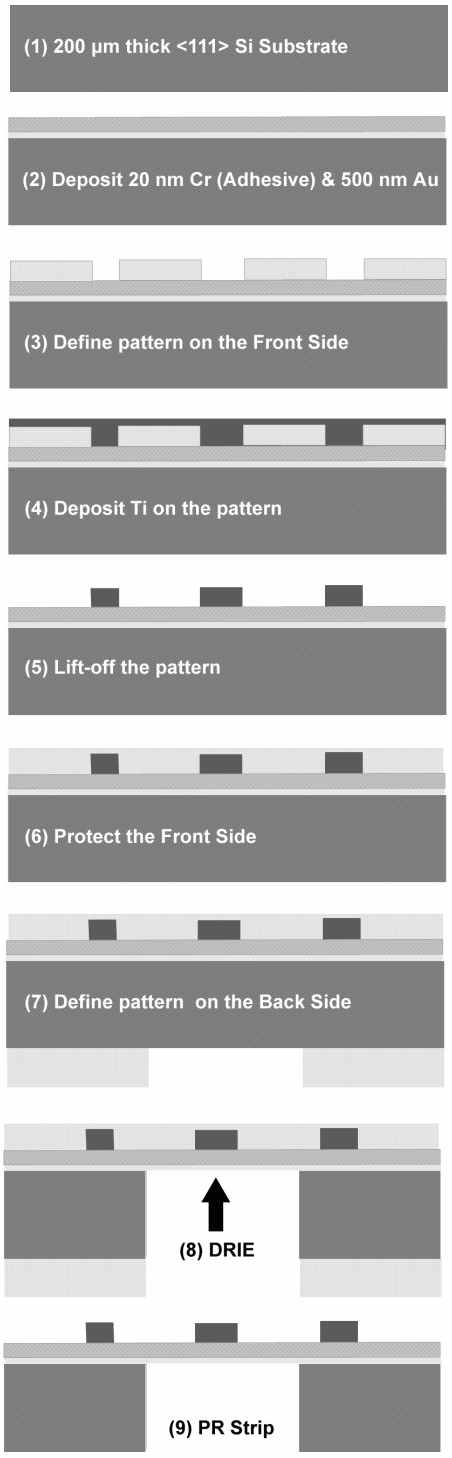

Figure 3.2: Microfabrication Process Flow

3.1.4. Final Products: Chips

Free standing gold diaphragms suspend over etched windows opened on a silicon chip as depicted in figure 3.3 (a). An edge of the square is 1.2 cm and the diaphragms are located around the center. The diaphragms are designed as slim rectangles with an aspect ratio of 10:1. The edges of the diaphragms are parallel to the edges of the chip. The chip is located at the center of a circular aluminum plate which has a 9 mm wide hole keeping the chip in contact with the pressurized fluid. The area that is exposed to hydraulic pressure is indicated by a discontinuous circular line in figure 3.3.

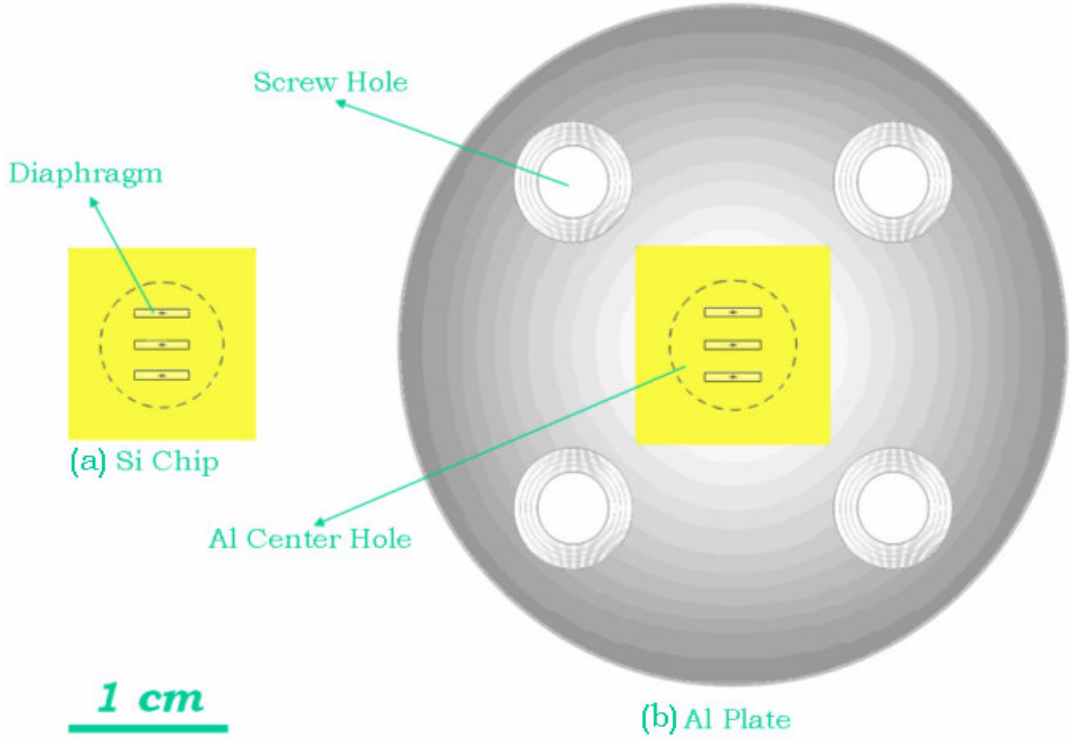

Figure 3.3: (a) Test Chip (b) Al Plate with Chip

3.2. Experimental Procedure

3.2.1. Chip Cleaning

After fabrication, the diced chips are stored in a Petri dish where they lay upon a sticky blue foil. The foil is torn with a razor and the chips are slowly peeled from the foil with Teflon tweezers. Each chip is cleaned before getting glued onto a circular aluminum platform. Initially, a chip is rinsed with acetone and the protective photoresist layer on the metal surface is removed. One can see the red PR layer gradually peeled and dissolved in acetone (figure 3.4. (a)). Immediately after the first bath, the chip is rinsed with alcohol in order to avoid the acetone drying on the metal. Finally, the chip is submersed in DI water and then dried with N_2.

3.2.2. Plastering

The clean chip is attached at the center of a clean Al plate. One should be careful to align the chip ensuring that the diaphragm of interest will be completely exposed to hydraulic pressure. The four screw holes can be used as reference points during positioning. If each corner of the chip is equally away from the neighboring hole, one attains the perfect alignment. High precision alignment of the sample (section 3.2.4) will be much easier as long as the square chip is symmetrically centered on the circle.

Epoxy adhesive is applied on aluminum surface along the edges of the square chip (figure 3.4 (b)-(c) & 3.5). It is prepared via mixing equal volumes of a resin and a curing agent. The mixing and casting of the viscous epoxy on aluminum is assisted by a needle. The adhesive becomes gel-like approximately 3 minutes after mixing. The curing of the epoxy stagnates approximately after 30 minute. This period varies if the fractions of mixture deviate from the ideal one to one ratio.

There are significant considerations for sticking the chip on aluminum surface. One should cast the adhesive merely on the aluminum surface, not on the chip. The viscous liquid will gradually spread on the close neighborhood of the edge of the square until the epoxy is gelated. The excessive amount of adhesive applied on the sample is undesirable since it might spread on the far inner regions towards the diaphragms. Epoxy should not be applied under the chip between the silicon-aluminum interface either; if so, the silicon is bended as solidifying epoxy experiences a phase change. Such a change at the interface affects the topography of the gold and should be avoided.

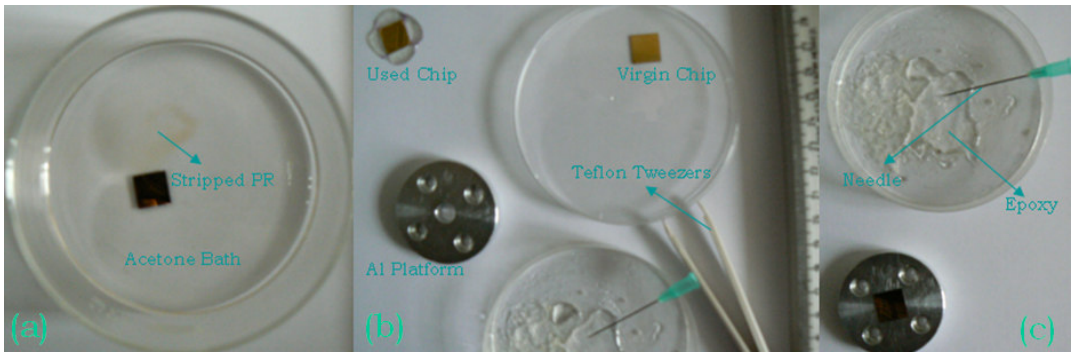

Figure 3.4: (a) Chip Cleaning, (b) - (c) Plastering

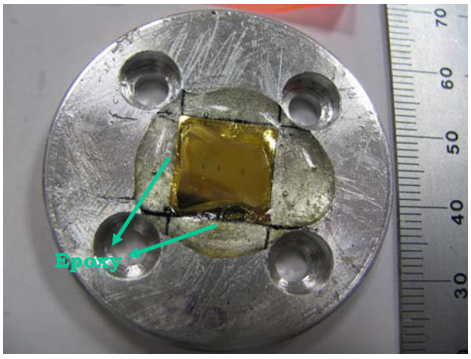

Figure 3.5: Square Chip Plastered on Al Plate with Epoxy

3.2.3. Clamping and Alignment

As long as the epoxy is hard, the aluminum platform can be clamped to the test machine. There are two significant considerations in this process:

1. During clamping, the diaphragms should not be extensively loaded, permanently deformed or contaminated.
2. At the end of clamping, there should not be any air bubble entrapped in the fluid chamber.

A piece of paper adhered between the Al plate and the chamber hole securely facilitates sample clamping. The procedure basically consists of three major steps:

1. The open fluid chamber should be completely filled with oil removing entrapped air out.
2. The backside of the Al plate should be filled with oil and closed with a piece of paper.
3. The Al plate should be put on the chamber and the paper is removed smoothly out along the plate-chamber interface.

During the placement of Al platform, the experimenter should vigorously hold it tight on the set-up to prevent air entering the closed chamber. Meanwhile, the experimenter should ensure that the sample is not loaded extensively. For this reason, a voltmeter is serially connected to the pressure sensor continuously indicating the amount of fluid pressure in the chamber. 1 Volt or higher increments in the signal may permanently deform the smaller diaphragms.

The experimental preparation is a significant step in bulge test analysis. One should carefully apply the nine steps listed below along with the security regulations encountered above. The nine steps of experimental preparation are demonstrated in figure 3.6.

1. All plumbs are closed and the chamber is completely filled with machine oil. The chamber is inspected for bubbles with a fiber-optic torch. The pressure sensor and the corresponding voltmeter are turned on.

2. The small space at the backside of the Al plate is slowly filled with oil until the level of the liquid advances the black O-ring located on the Al surface.
3. Oil in the small space is carefully enclosed with a piece of paper ensuring that there is no air remained beneath the insulator paper: Observe that O-ring and paper strongly stick each other along wet environment. The paper should remain attached even after the plate is turned downside-up.
4. The Al plate is vertically put on the set-up without releasing the force applied on it. Remember: If the plate is tilted, the paper will peel and the previous steps should be repeated.
5. A plumb is opened before the interfacial paper is removed. The signal in the voltmeter drops to the reference value *i.e.* ~1 V and remains constant. In this way, the experimenter prevents the risk of extensive loading.
6. Tightly holding the Al plate, one can pull the interfacial paper out.
7. The screws are gradually fastened in diagonal sequence. The plumbs are closed and the chamber is inspected whether there is any bubble trapped inside or not.

3.2.4. High Precision Alignment

The steps (8) and (9) consist of high precision alignment. After sample is clamped on the main body, freely moving test set-up is brought under the laser sensor which is clamped on a fixed boss attached onto a vibration table. Initially the sample is roughly moved along by hand but this is not sufficient for accurate positioning.

The experimental procedure continues as follows: The laser sensor and camera is turned on along with TV. The camera magnifies and screens the area around the point where the laser beam falls upon. Light is carried by the fiber optic torch onto the sample surface. As the experimenter sees the laser point, the surface is scanned by the motion of mechanical actuators attached at the carrier stages. In the mean time, the relative position of the surface with respect to the fixed position of the sensor is interpreted via a

voltmeter. This voltmeter is serially connected to the laser sensor and allows one to observe the experiment together with the voltmeter connected to the pressure sensor.

In order to achieve the perfect alignment of the sample, one should read the same voltage value along the chip surface. If the sample is tilted, one requires to align the sample around the rotating axes of the set-up. The two significant actuators controlling the rotating axes are shown in section (8) of figure 3.6. The actuators that control the scanning motion are shown in section (9) of the same figure. Due to the dust particles and leftover photoresist, it is hardly possible to attain the perfect alignment. Nevertheless, an experimenter can achieve close to perfect alignment as long as an iterative effort is practiced among the scanning and aligning processes.

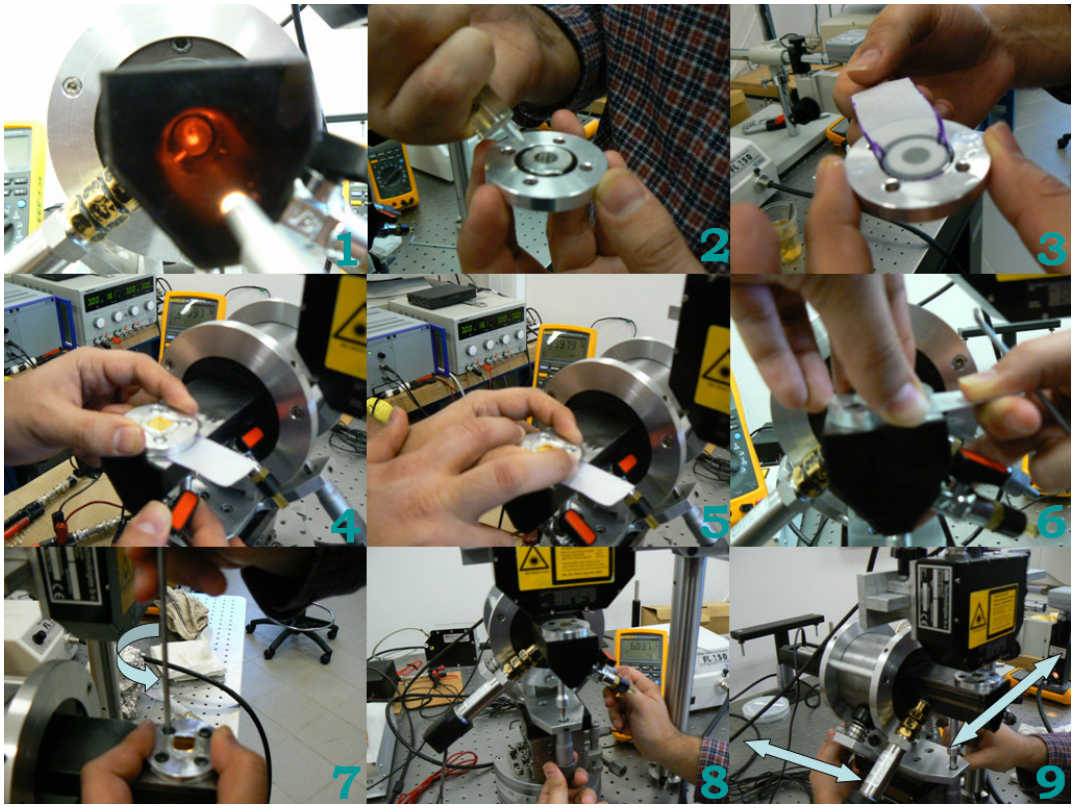

Figure 3.6: Experimental Procedure: Sample Clamping (1-7) & Alignment (8,9)

3.2.5. Before the Experiment

There are few other tasks to accomplish right before the experiment. The Labview program (figure 4.1) requires some parameters to be specified such as the diaphragm size, the rate of the experiment and other hardware parameters for data acquisition. Prior to assigning the control parameters of the measurement, the experimenter should decide to choose the diaphragm to perform the experiment. When the diaphragm is chosen, the piezo actuator is turned on and then the plumbs are closed respectively. The close vicinity of the center of the diaphragms is scanned with the laser and the flatness is ensured (Remember: h_0 is set to zero in equation 2.6). The laser probe is moved on the center of the diaphragm which is indicated by a 10 nm thick titanium cross '┼' microfabricated on the gold surface. The cross in the center of a 380 μm ($2a$ = 380 μm) wide diaphragm can be seen in figure 3.7.

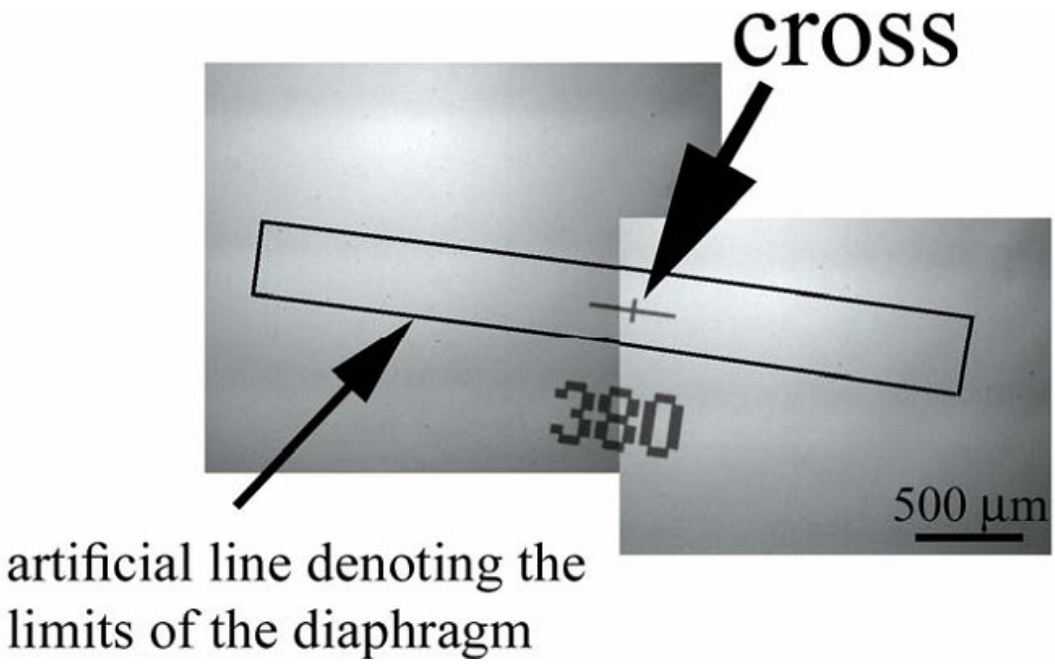

Figure 3.7: The Optic Microscope Image of a 380 μm wide Au Diaphragm

3.2.6. After the Experiment

The experiment is automated by a Labview routine which can be modified to actuate the piston in different modes and take data at various acquisition rates. The details about data acquisition and automation will be discussed at the next chapter. At the end of each experiment, the aluminum platform should be unclamped and slightly freed from contaminated oil by a diaper. The sample should be labeled and kept in a safe storage until further characterization techniques like electron microscope analyses are performed. The chamber should not be kept enclosed for long times, otherwise the pressurized high pressure causes relaxation of the insulator set-up components and fluid may leak through the connective sites. Such a problem has been once experienced and the set-up was re-maintained.

Chapter 4

DATA ACQUISITION, AUTOMATION & DATA PROCESSING

4.1. Data Acquisition

4.1.1. DAQ Card

A DAQ card is the interface between a computer and an experimental environment allowing one to automate various tasks simultaneously and take experimental data. In the bulge set-up, the sensors and the actuator are controlled via a National Instruments DAQ card connected to a PC. The card can be driven by Microsoft Windows compatible software, Labview, which can facilitate virtual instruments in a PC environment. The DAQ card consists of ten input and two output female BNC connectors that can communicate with sensors and actuators respectively. The card can transmit signals between a host computer and connected devices. 10 Volt is the threshold value for transferred signals. Therefore, sensors are constrained to give outputs smaller than the threshold value; such that the output of pressure sensor is confined between 0.99 and 4.96 Volts while the output of displacement sensor remains between 0 and 8.91 Volts. For details, please refer to section 2.4.

4.1.2. Labview

Labview routines are graphical program codes. Each Labview routine is composed of two main windows, the front panel and the block diagram. The front panel is the user interface of a Labview routine consisting of control buttons, indicators, charts and

graphs. One can control or monitor an experiment working on the front panel of a Labview routine. The charts, icons and other user-interfacial components of a virtual instrument can be modified editing the front panel. On the other hand, the block diagram is a graphical programming media where logical and mathematical arguments along with readily available subroutines compose program algorithms. The functions of a Labview routine are sequentially wired (connected) to each other either collaboratively working or independently running within loops or case structures. One can build many applications using Labview; nevertheless, data acquisition is the most fundamental facility that is widely used by experimenters.

Experimental conditions of the bulge test can be modified via using different actuation mechanisms. The DAQ process can be modified for each distinct experiment as well; however there is no need to change optimized DAQ specifications once the uncertainty of routine experimental results is minimized. In the bulge project, the data scan rate is always set to 200 scans per second while 50 scans are written to an identical separate sheet at each time. Thus, the program is synchronized to run 4 times per iteration sweeping the whole scan backlog in the buffered memory.

There are two distinct Labview routines used for bulge analysis: the first one (figure 4.2) is used for system calibration whereas the second one (figure 4.3) automates the system to achieve a constant strain rate condition. Both routine uses the same data acquisition method, while each has a different way to drive the actuator. The calibration routine is dedicated to determine the ratio between the signal that drives the actuator and the signal generated by the motion of the test membrane (see section 4.2.1). In contrast, the main routine implements the time dependent function generated by the static system parameters. The Labview representation of this function can be seen in the block diagram (figure 4.3) at the right hand side of page 33. The detailed derivation of this function is given in section 4.2.3 starting at page 38.

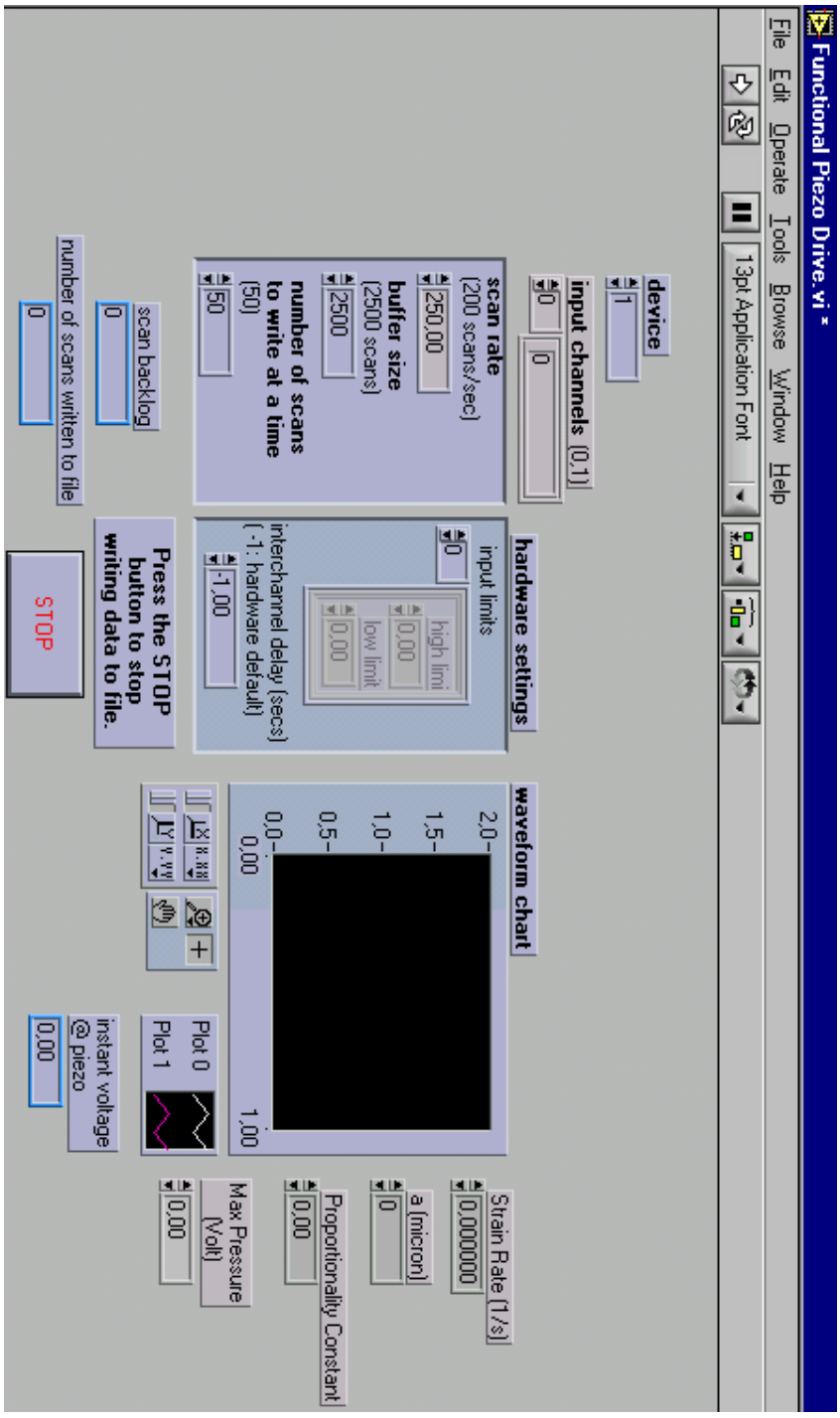

Figure 4.1: The Front Panel of the Main Routine

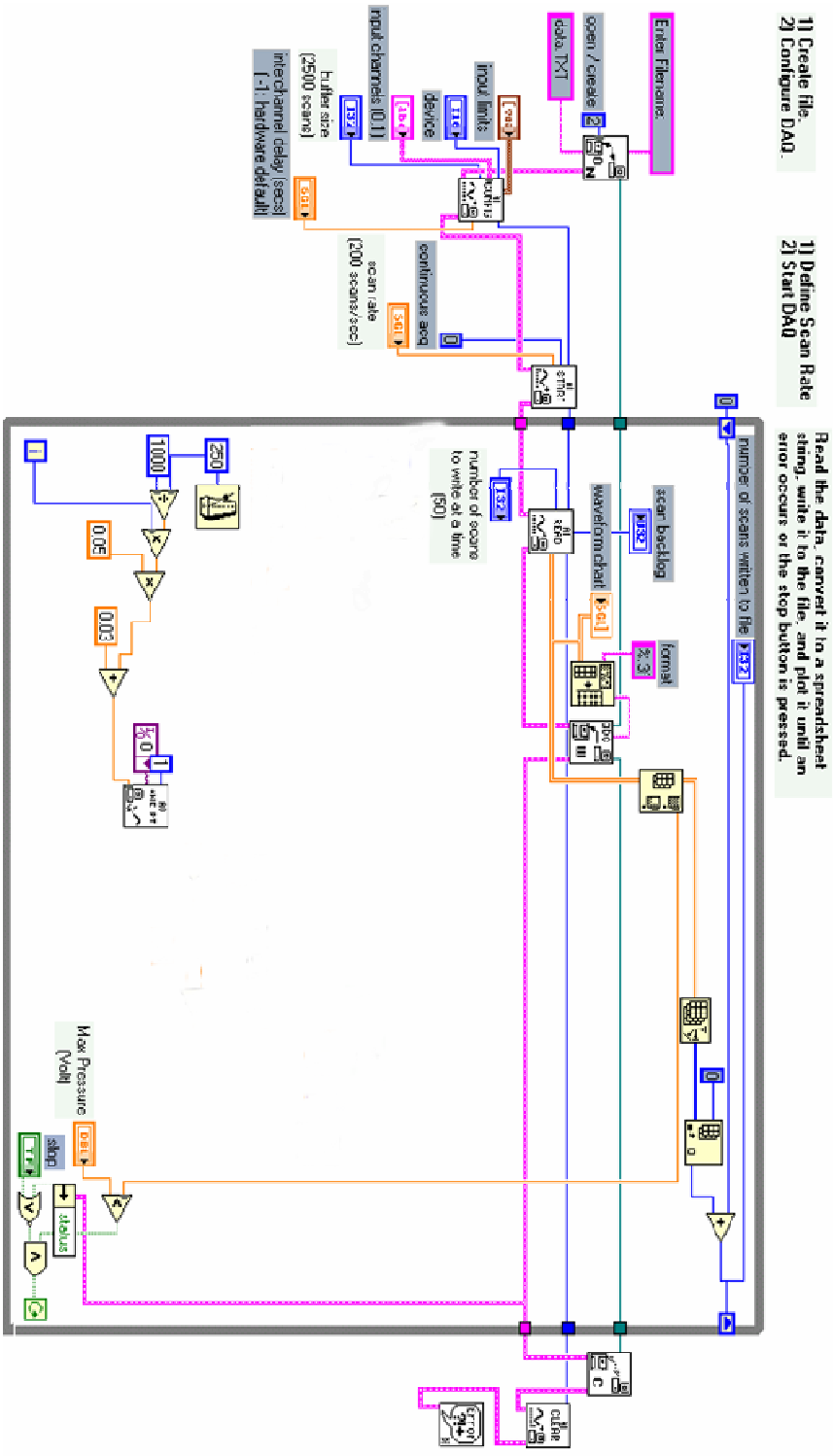

Figure 4.2: Block Diagram of the Calibration Routine

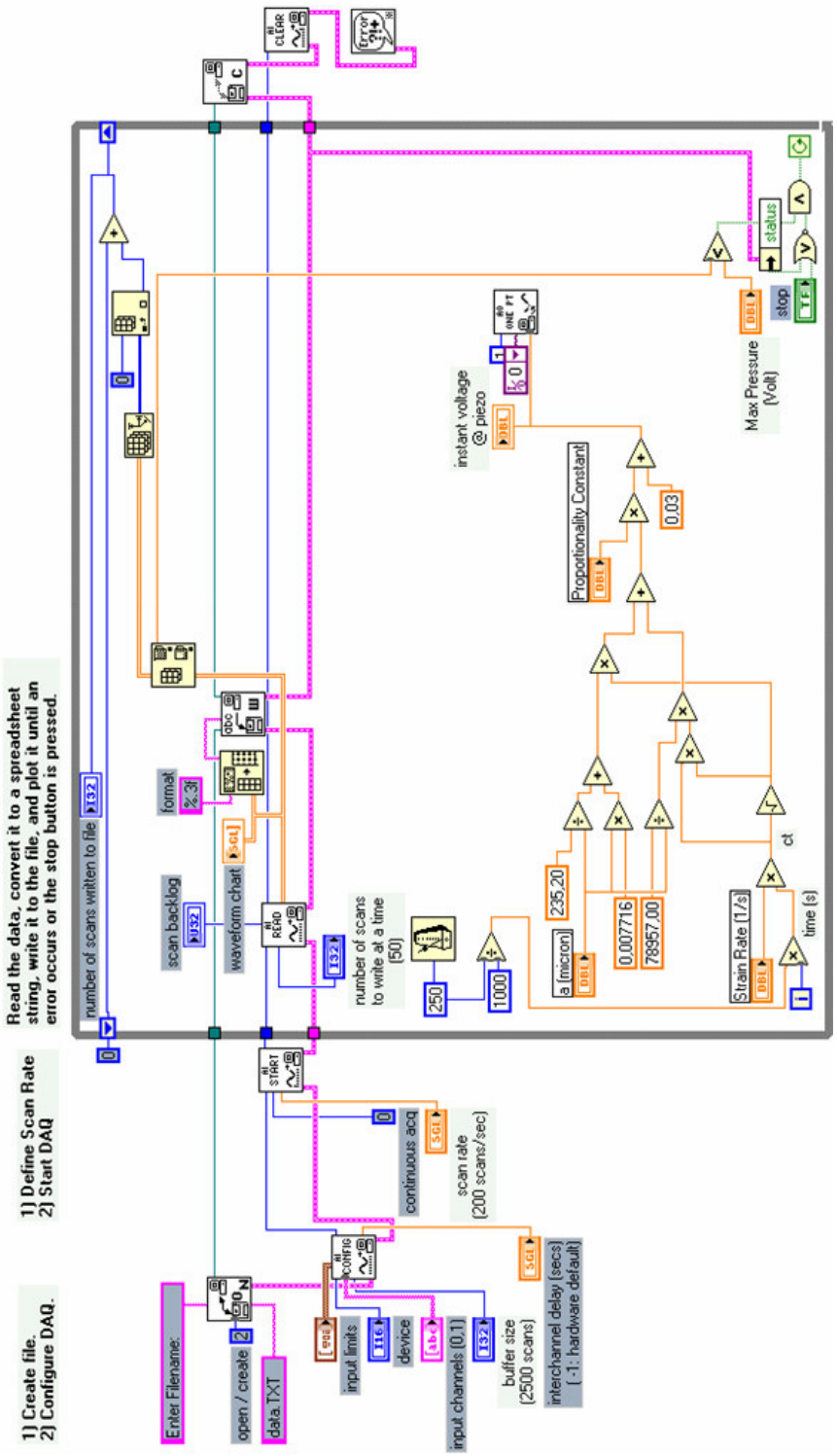

Figure 4.3: Block Diagram of the Main Routine

4.2. Automation

4.2.1. The Static System

There can be several ways to adapt bulge test into a controlled strain rate analysis. One can solve the issue using either a dynamic model or static analysis. Dynamic modeling requires system identification, a series of experiments measuring the frequency response of a system as a result of varying stimulus. Having an identified system, one can establish the transfer function for a controller of interest. Such an effort was initially practiced via designing a PID controller. However, the system identification is not precisely accomplished due to the noise in displacement data. Besides, the high order time dependence of the assigned set function, *i.e.* equation 4.7 requires two controllers (a PID and a PI) to be performed collaboratively. Such a complicated approach failed to create a well-situated solution for the constant strain rate problem.

Instead of a dynamic approach, the static analysis has been a more suitable solution to the constant strain rate problem. In order to suggest such a solution, the static response of the system under monotonic stimulus effect is characterized. For this purpose, a Labview calibration routine is designed (figure 4.2). The relationship between the controlled rate of piezo input and accompanying displacement output is determined. The response of the laser sensor is shown to be linearly proportional to monotonically increasing piezo signal. The coefficient of linearity is found to be approximately 40 ± 5 for each rate of piezo drive (Table 4.1). In other words to say, the output sent to pizeo by a DAQ card creates a 40 fold smaller input that is generated by displacement sensor. Therefore, one can control received laser signal h manipulating the time dependent $\delta(t)$ signal driving the piezo actuator. See Table 4.1 for some calibration data.

$$h(t) \cong \frac{\delta(t)}{40} \tag{4.1}$$

Table 4.1: Examples of Static Calibration

dδ/dt **Piezo Rate [V/iteration]**	*dh/dt* **Displacement Rate [V/iteration]**	*dδ/dh* **Proportionality Constant (~40)**
0.03	0.000701405	42.8
0.10	0.002735425	36.6
0.30	0.007818417	38.4

Before each experiment, the samples are calibrated by the Labview routine shown in figure 4.2. At the end of each calibration, the experimenter attains the exact value of the proportionality constant for a diaphragm of interest. However, it is not a rough approximation to take this constant 40 since the proportionality is not extensively rate dependent[1].

4.2.2. Substrate Deflection

In an ideal bulge test, diaphragms should suspend over rigid windows so that the pressurized fluid cannot deflect the experimental frame. Figure 4.4 depicts an explanatory view of the ideal and actual cases in substrate stiffness. In this project, the gold diaphragms are micromachined on 200 micron thick Silicon wafers (section 3.1.1). Such a thickness is required due to microfabrication constraints; but, on the other hand, stiffness deprivation results in other complications. Applied pressure causes considerable amount of substrate deflection which apparently creates handicap in direct retrieval of useful data. Displacement of substrate should be eventually subtracted from measured deflection.

Delamination is the second concern in the reliability check of the deflection data. In order to inspect the possibility of delamination, two sets of experiments are performed.

[1] Other calibration experiments which are not recorded and hence excluded from Table 4.1 show similar static response.

First, a routine experiment is performed in which the displacement data is taken from the close vicinity of the edge of a diaphragm (figure 4.5 (i)). The deflection is measured approximately 1.2 μm. At the same experimental conditions, the total displacement of the center of the diaphragm is measured as 6.0 μm. The net deflection is found approximately 80 % of the total measured deflection. In the second set of experiments, a sample is prepared upside down and a final measurement is taken over the silicon surface. Similar deflection behavior is observed (figure 4.5 (ii)) proving that the out-of-membrane-disposition is not due to delamination; instead, there is pure substrate deflection that should be excluded from the measured data. The adhesive Cr layer deposited between Si and Au successfully rules out delamination risk.

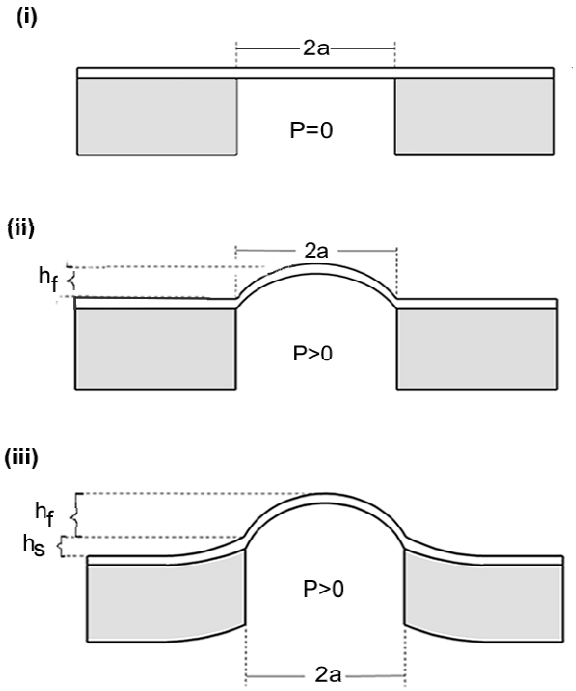

Figure 4.4: (i) No deflection, (ii) Rigid Substrate, (iii) Non-rigid Substrate

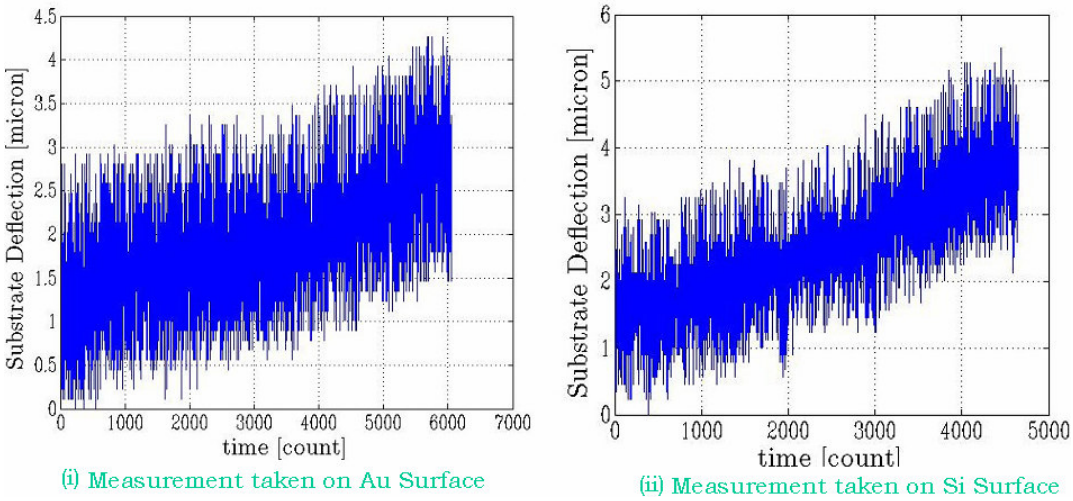

Figure 4.5: Substrate Deflection Measured on (i) Backside, (ii) Frontside

As a limitation of the single point displacement measurement, the deflection of the substrate and the deflection of the membrane cannot be determined simultaneously. Therefore, at the end of each regular measurement taken on the center of the diaphragm, the experimenter needs to run another experiment measuring the deflection of the substrate at the same experimental conditions. Briefly, using the current infrastructure, the net deflection of the membrane (h_f in fig. 4.4) can be merely determined via subtracting the substrate deflection data (h_s in fig. 4.4) from the total measured deflection data ($h_s + h_f$ in fig. 4.4).

In order to remove the substrate deflection from the total displacement of the diaphragm, a rather simple method was discovered. Simulations (figure 4.6) along with the experimental results (figure 4.5) showed a linear relationship between the substrate deflection h_s and the applied pressure P as outlined in equation 4.2.

$$P = \alpha h_s \tag{4.2}$$

Measuring the linear proportionality constant α, an experimenter can numerically determine the net deflection of a bulging membrane. The value of α is retrieved from

the linear fit of the pressure vs. substrate deflection graph. The typical value of experimental α is determined on the order of 10^9 Pa/m. In order to verify this quantity, a series of FEM analysis is performed. A 500 μm wide gold membrane with 55 GPa Young's Modulus, 0.425 Poisson's ratio and 130 MPa biaxial residual stress is located over the center of a 1 cm radius Silicon substrate. Poisson's ratio and Young's modulus of Silicon is taken 0.25 and 160 GPa respectively. Two major deviations from the actual chip design existed in this model. First, the effect of neighboring diaphragms is not taken into account. Second, the diaphragm width is taken fixed which indeed varies from one chip to another. Nonetheless, the simulation value of α is determined to be $3.28*10^9$ Pa/m which appears to be quite compatible with the experimental α values.

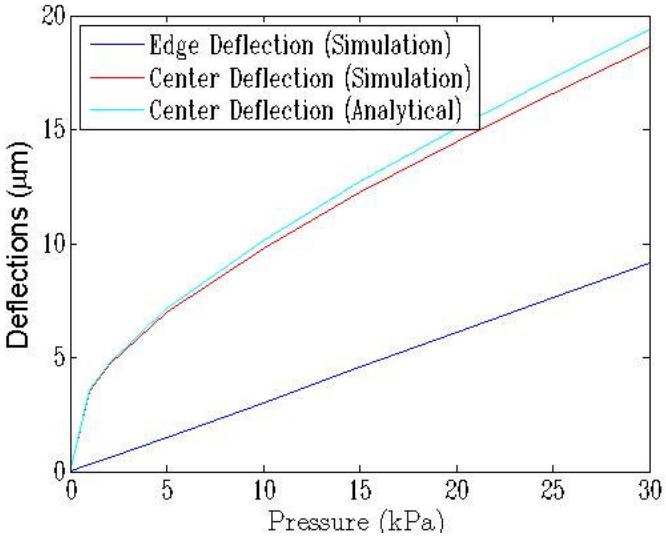

Figure 4.6: Simulation Results for a 500 μm wide Diaphragm

4.2.3. Updated Constant Strain Rate Condition

Since measured center displacement of the membrane is not the net deflection of the free standing film, the automation facility controlling the strain rate should be upgraded. For this purpose, some results from the previous sections should be reviewed together.

Initially, one should take into account the significant remark related to the substrate behavior. Rearranging the equation 4.2 substrate deflection can be represented in terms of variable pressure

$$h_s = \frac{P}{\alpha} \tag{4.3}$$

In the elastic regime, pressure can be represented in terms of material constants, membrane geometry and film deflection. Factorizing equation 2.2 with $1/\alpha$, equation 4.3 is given the following form:

$$h_s = \frac{P}{\alpha} = \frac{2}{\alpha}\frac{\sigma_0 d}{a^2}h_f + \frac{4}{3\alpha}\frac{Ed}{(1-\nu^2)a^4}h_f^3 \tag{4.4}$$

The total measured deflection of the membrane h_t is the sum of the substrate deflection h_s and the net film deflection h_f

$$h_t = h_s + h_f \tag{4.5}$$

Finally, the equation 4.4 can be modified as a representation of the measurable parameter h_t and the parameter of interest h_f

$$h_t = h_f + \frac{2}{\alpha}\frac{\sigma_0 d}{a^2}h_f + \frac{4}{3\alpha}\frac{Ed}{(1-\nu^2)a^4}h_f^3 \tag{4.6}$$

Remember equation 2.7: The net film deflection h_f should have square root time dependence in order to ensure a constant strain rate condition. Therefore, the valid constant strain rate behavior of the measured displacement signal should have a time dependency as in the following form:

$$h_t = \left[\left(\frac{\sigma_0 d}{a\alpha} + \frac{a}{2}\right)\sqrt{6c}\right] t^{1/2} + \left[\frac{Ed}{(1-\nu^2)a\alpha}\sqrt{6c^3}\right] t^{3/2} \qquad (4.7)$$

This relationship does not guarantee to secure a constant strain rate behavior beyond the yield stress. Nonetheless, it is implemented to the main Labview routine till the piston stops its monotonic motion. This mechanism has been sufficient to determine the strain rate dependent yield strength of the gold membranes. In the implementation of the Labview routine, Young's modulus (E=55 GPa), Poisson's ratio (υ=0.425) and residual stress (σ_0=130 MPa) are assumed approximated values referring to the previous elastic measurements and the literature. The simulation value 3.28 10^9 Pa/m is assigned for α which shows to be an acceptable approximation for each measurement. Thickness d is taken 500 nm for each measurement. In addition to the invariable parameters, there are two control variables in the Labview model. The width of the membrane $2a$ and the strain rate c values should be assigned prior to testing.

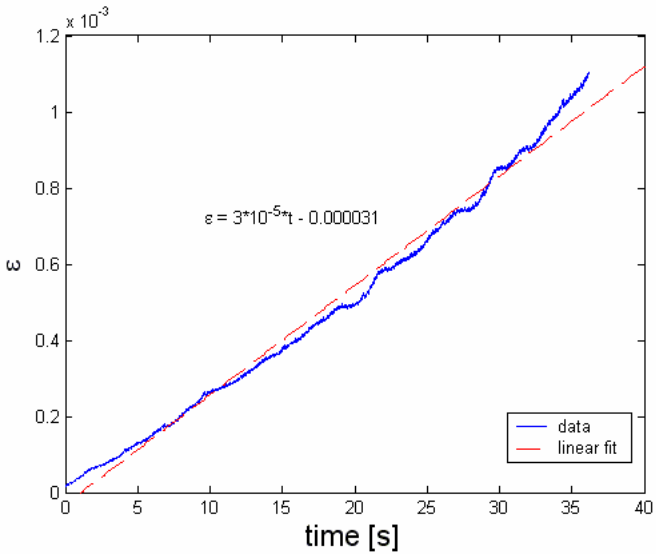

Figure 4.7: Strain vs. Time graph for a 320 μm wide diaphragm

The accuracy of the approximated parameters is reflected to the consistent linear behavior in the resultant strain vs. time graph of a 320 μm wide diaphragm in figure 4.7. Notice that there is a slight deviation from the linearity towards the end of the curve where the material is in the plastic regime.

4.3. Data Processing

4.3.1. Filtering Raw Data

Specular reflective sensing is a useful method to measure translational displacement in microscale. It requires a source of monochromatic light and a reflective surface. In the bulge test, a red laser is reflected at the center of a rectangular gold membrane. The geometry of the bulging membrane resembles a cylinder. The laser spot ideally falls upon along the vertical axis of that cylinder. However, 10-20 micron wide laser spot exceeds to the cylindrical arc scattering away from the reflective sensor. The scattering of the reflection produces deviations in the analog signal. Therefore, broad fluctuations in the displacement data occur such as the ones in figure 4.8. The inevitable fluctuations along with the low resolution ability of the sensor dramatically affect the quality of the measurements. After failing to vanquish the noise in the signal by employing additional hardware settings, a numerical tool is exploited to reduce the uncertainty in the received data. For this purpose, filtering modules of MATLAB is used.

The filtering is merely applied along the displacement column of data without changing pressure value of the same indices. The number of data remains constant during each filtering operation. The basic functionality of filtering is the accumulation of the scattered points around a mean value. One can see the similarity in the trends of a raw data and its filtered version in figure 4.8. The blue region shows the scattered raw data in voltage form and the red line is the filtered version of it. The well identified

minimum of the filtered data allows one to normalize *P* vs. *h* graphs to the origin. Please see the Appendix for the MATLAB routine used for filtering.

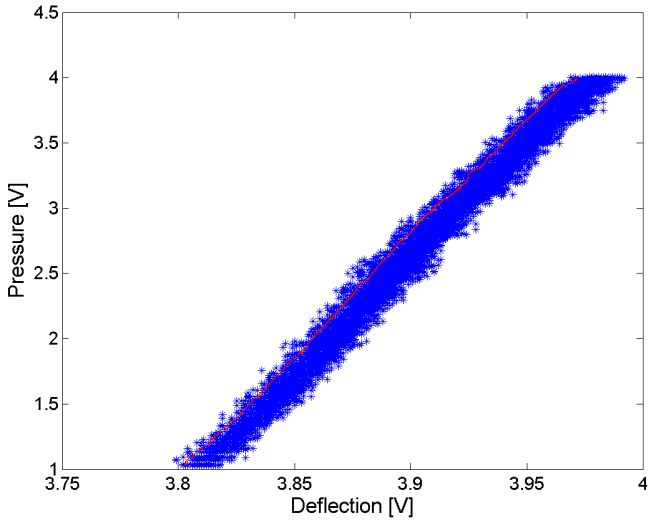

Figure 4.8: Pressure vs. Deflection Graph of the 320 μm wide Diaphragm

4.3.2. Determination of Net Deflection

The details related to the substrate deflection are discussed in section 4.2.2. One needs to subtract the substrate deflection from the measured deflection in order to retrieve the net displacement of the membrane. There is a significant relation outlined in equation 4.3, which can be exploited to simplify the subtraction task.

The linear proportionality constant α is measured for each experimental condition prior to the actual testing. The Labview routine provided for calibration is used for this purpose and the substrate behavior can be determined for various constant rates of piezo drive. Two sets of substrate deflection data is retrieved from the two distinct edges of the diaphragm. Slopes of the two corresponding sets of data are determined by linear curve fitting. The arithmetic mean of the two slopes gives the desired α value.

The α value is recorded for the numerical subtraction. Then, the actual test is performed and the total displacement of the composite system is measured at the center

of the diaphragm. Finally, linearly varying substrate behavior is numerically subtracted from each filtered total displacement using the corresponding pressure data:

$$h_f = h_t - \frac{P}{\alpha} \tag{4.8}$$

Figure 4.9 shows the net deflection h_f and total deflection h_t curves of a 320 micron wide membrane loaded with 3 10^{-5} s^{-1} strain rate.

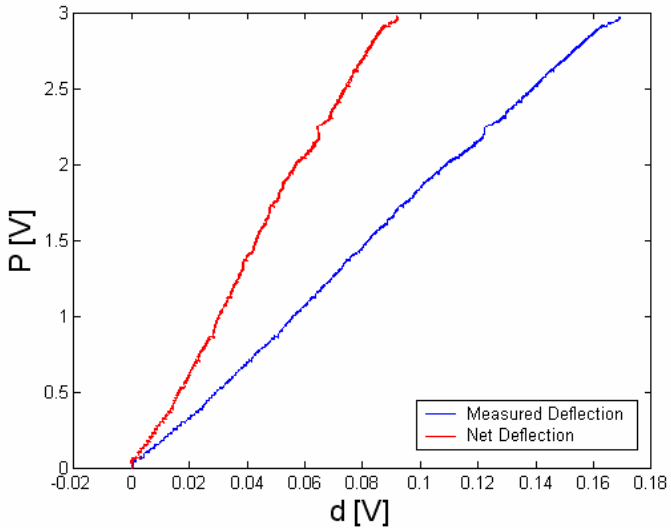

Figure 4.9: Pressure vs. Net Deflection Graph of the 320 μm wide Diaphragm

4.3.3. Stress vs. Strain Diagrams

The net deflection-pressure data can be converted to stress vs. strain diagram using equation 2.4. Since the initial analytical model does not consist of residual strain ε_0, the resultant graph looks like the one in figure 4.10 (i). If the curve is shifted along the strain axis, the complete stress vs. strain diagram resembles figure 4.10 (ii).

Having the strain data, one can plot the strain vs. time graph (figure 4.7). The strain rate of the experiment can be determined applying linear fit to this graph. Approximately 5% of the initial and the final portion of the data are wasted due to broad fluctuations and filtering errors. Therefore these portions are excluded from the stress vs. strain graphs presented in the next chapter.

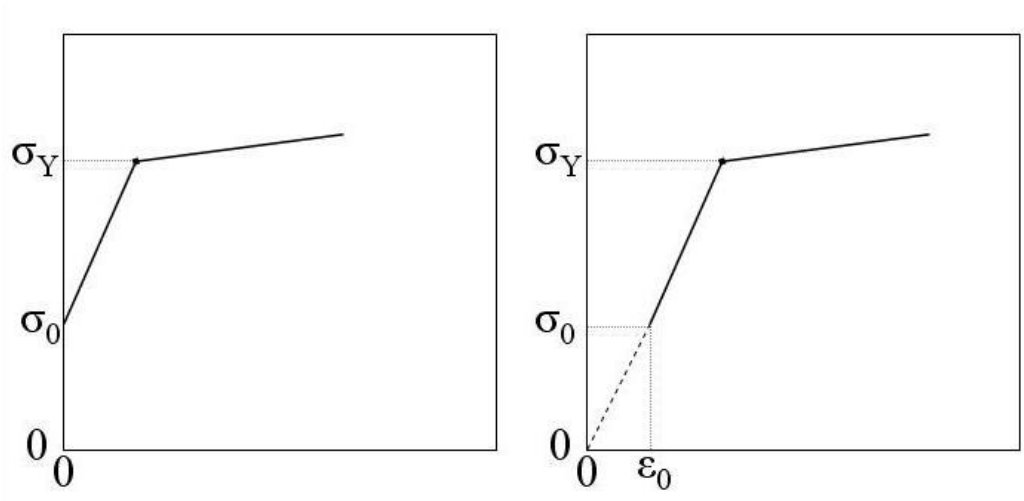

Figure 4.10: (i) Measurable Diagram (ii) ε_0 shifted-Ideal Diagram

Chapter 5

RESULTS & DISCUSSION

5.1. Overview

There has been an increasing trend to inspect strain rate dependent mechanical properties of gold films. Emery *et al.* studied the tensile behavior of free standing gold films with coarse grained [40] and fine grained [41] structures. Evaporated gold with grain size of 400 nm and smaller showed strong rate dependent yield behavior while coarser grained material remained unaffected. In a similar study of Chasiotis *et al.* both evaporated and electrodeposited nanocrystalline gold films showed strain rate dependent plastic behavior [11]. Although constant strain rate loading case could not be accomplished, in a later study [42] the mechanical tests of evaporated gold films showed that the yield strength of nanocrystalline metal is highly rate dependent. Such a behavior has not been observed in bulk metals indicating that there might be a correlation between the grain size of a metal and the rate dependency of strength.

The microstructure and mechanical behavior of metals varies due to dramatic changes in their film thickness [3]. As the grain size gets smaller typical Hall-Petch like strengthening behavior is observed in gold [41-43]. Below a certain grain size microfabricated gold can experience high temperature plastic recovery [12] and lower stiffness [23]. Furthermore, the interfacial effect can confide gold in certain crystallographic texture changing the effective elastic modulus [11, 43]. Table 5.1 summarizes the results of some significant experimental efforts investigating the mechanical properties and material specifications of gold thin films.

Study	Sample Type	thickness [μm]	grain size [μm]	texture	ε̇ [s⁻¹]	σy [MPa]	E [GPa]	Study	Sample Type	thickness [μm]	grain size	texture	ε̇ [s⁻¹]	σy [MPa]	E [GPa]
Chasiotis *et al.* (2006) Tensile	Electroplated	2.80	0.20		1*e-2	270	35	Emery *et al.* (2002) Tensile	Thermal Evaporation As-Deposited	0.80	0.58		6*e-5	340	
			0.20		1*e-3	220	35			1.60	0.71		6*e-5	239	
			0.20		1*e-4	155	35			2.10	0.56	111	6*e-5	212	
			0.20		1*e-5	70	20			2.00	0.48	111	6*e-5	239	84/88
	Evaporated	0.50	0.10		1*e-3	240	35		Thermal Evaporation Annealed	1.90	0.66		6*e-5	271	
			0.10		1*e-4	220	35			1.60	1.14		6*e-5	142	
			0.10		1*e-5	170	35			2.10	1.46		6*e-5	89	
			0.10		1*e-6	140	20			1.60	5.98		6*e-5	42	
	Evaporated	0.65	0.10		1*e-3	295	35			2.10	5.67		6*e-5	36	
			0.10		1*e-4	280	35			2.00	1.19	111	6*e-5	130	
			0.10		1*e-5	285	35			1.90	1.07		6*e-5	199	
			0.10		1*e-6	180	20			0.25	0.26		6*e-5	384	
Wang *et al.* (2008) Tensile	Evaporated	0.25	0.04	111	2*e-4	390	58	Emery *et al.* (2002) Tensile	Thermal Evaporation As-Deposited	0.25	0.15		6*e-5	390	
					1*e-4	368	59						7*e-6	273	
					5*e-5	308	58			0.80	0.19		6*e-5	426	
					2*e-5	275	59			2.10	0.20	111	5*e-5	434	
					2*e-6	230	54						1*e-6	230	
		0.50	0.05		5*e-4	365	52			0.23	0.13	111	6*e-4	455	
					2*e-4	330	51						6*e-5	360	71/56
					4*e-5	313	52						7*e-6	236	63/50
					1*e-5	275	52						5*e-4	474	
					5*e-6	233	53								
		1.00	0.10		4*e-4	277	65	Wu *et al.* (2005) Bending	Electro-deposited Nanowires	0.70	0.17		7*e-5	377	79/61
					2*e-4	250	62						7*e-6	254	80/80
					7*e-5	235	63			Φ = 40	~40		N/A	5600	70
					2*e-5	237	63			Φ = 200			N/A	3500	70
					8*e-6	218	66								
Espinosa *et al.* (2003) Bending	Evaporated (e-beam)	0.30	0.25-0.30	111	6*e-5	220	53-55	Rajagopalan *et al.* (2005) Tensile	Sputtered	0.20	0.05	111	1*e-4	70	
		0.50			6*e-5	220	53-55								
		1.00			5*e-5	90	53-55								

Table 5.1: Properties of Gold

5.2. Elasticity Analysis

There are two methods to determine elastic properties from bulge tests. One can apply least squares method to fit a cubic polynomial equation for the pressure-net deflection data. The properties of interest can be calculated from retrieved polynomial constants. In this method, the experimenter should avoid taking data beyond elastic region where the polynomial relation given by equation 2.1 loses its validity. Therefore, the membrane should not be loaded extensively.

The second method relies on the determination of stress vs. strain diagrams. The details of computing stress and strain out of raw data were already discussed in chapter 4. The slope of the initial linear region of the plotted diagram gives the plane strain modulus ($E/(1-\upsilon^2)$). Young's modulus can be trivially retrieved from plane-strain modulus taking the Poisson's ratio of gold films 0.425 [44].

In this study, Young's modulus and residual stress of the gold diaphragms are measured 51.1 ± 12.2 GPa and 134.8 ± 35.2 MPa respectively. The results given in table 5.2 are measured in various strain rate conditions between 10^{-5} and 10^{-4} s^{-1} range. Slower rates were not desired due to possible intervention of anelastic effects like grain boundary sliding [23]. Average Young's modulus of the thin films is calculated lower than the Young's modulus of bulk gold, *i.e.* 78 GPa. Such a difference was observed in similar studies [11, 42, 43] as well. The standard deviation in the elastic data is high because of the broad fluctuations effective especially at the inception of the measurements. Besides, in each elasticity and plasticity analysis, approximately first 10% portions of the data are deleted in order to achieve more precise results. The overall accuracy of the final result can be explained via studying the X-ray diffraction analysis of the film.

One can accurately estimate the Young's modulus knowing the exact crystallographic texture and compliance properties of Au. As a final characterization step, X-ray diffraction experiments were performed on gold samples. The theoretical and the experimental X-ray diffraction spectrums are given in figures 5.1 and 5.2

respectively. There is extreme texture in 38^o and 82^o peaks which correspond to <111> and <222> directions respectively. This result is expectable since {111} plane family has the lowest surface energy of the available configurations in the Au crystal [45]. A remarkable study of Espinoza *et al*. [43] showed that <111> dominated anisotropic texture in gold thin films consistently exhibits 53-55 GPa Young's modulus. Other studies offered an extensive variety of Young's modulus values with larger uncertainty. All these results for diversely fabricated Au samples remain within 20-88 GPa range verifying that our result is physically acceptable.

Table 5.2: Elasticity Measurements

a [μm]	E [GPa]	σ_0 [MPa]
180	54.0	95.8
180	49.4	97.7
180	55.8	92.0
180	41.5	95.2
180	61.7	69.2
160	40.3	139.2
240	46.1	188.7
240	53.2	171.3
240	77.9	154.0
240	48.4	198.1
240	35.3	124.6
240	59.4	126.9
240	61.7	124.3
310	51.8	151.2
310	62.3	146.0
310	47.9	151.2
300	29.3	159.3
310	40.8	158.5
300	28.3	190.3
240	52.0	143.6
240	74.2	115.4
180	50.2	99.2
160	40.3	82.2
160	64.2	162.4
Avg:	**51.1**	**134.8**
Std:	**12.2**	**35.2**

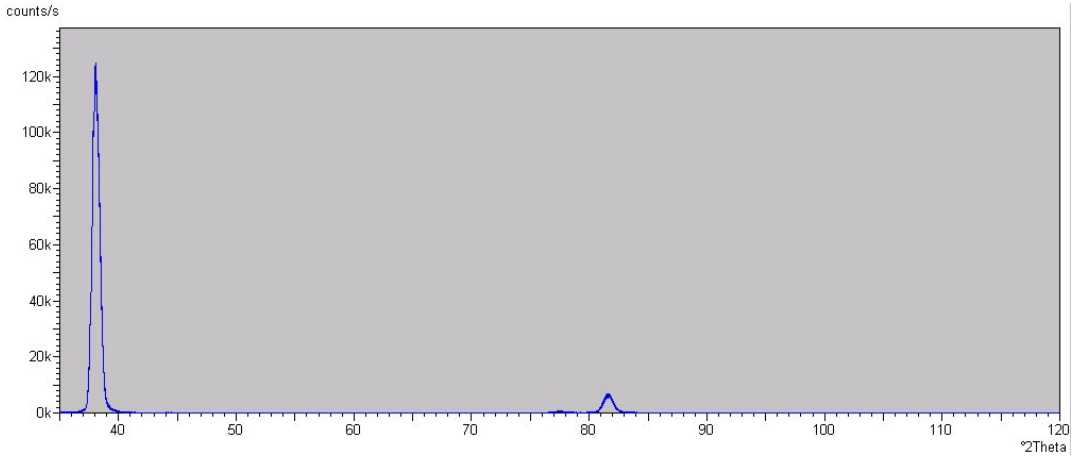

Figure 5.1: Theoretical X-Ray diffraction pattern for Au

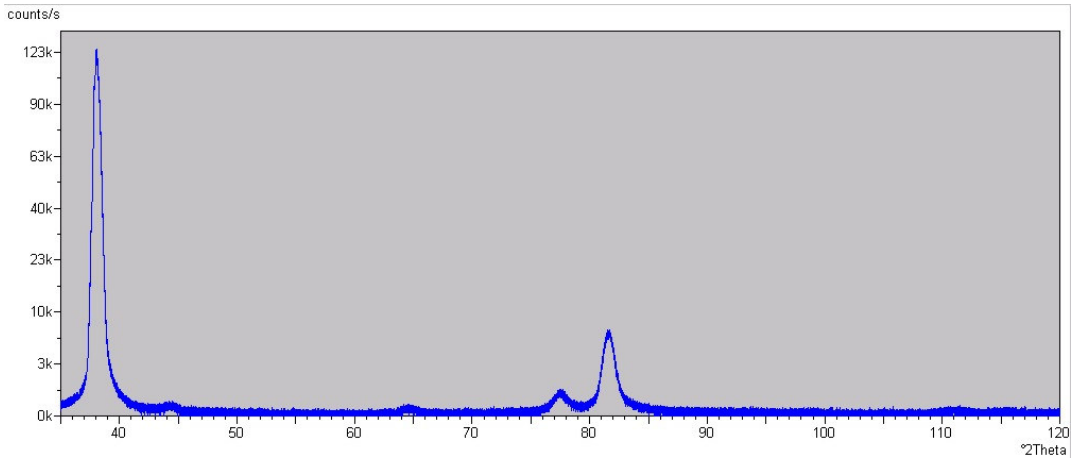

Figure 5.2: Experimental X-Ray diffraction pattern for Au

In the light of X-ray diffraction results, some other precious information regarding the microstructure of the sample can also be understood. For tested Au samples, the peak width is much wider in the experimental spectrum than in the theoretical one. There are various reasons for peak broadening such as the effect of experimental setup, dislocation activity, internal stresses and small grain size. Since plasticity in metals is dictated by dislocations, one can conclude that activated dislocations are highly abundant and their existence is effective on the final form of the X-ray results.

However, the current data is insufficient to have such a strict conclusion other than the actual crystalline texture.

5.3. Plasticity Analysis

Due to the limitations of the set-up, gold membranes could not be loaded till mechanical failure. The stress-strain graphs are plotted up to random points in the strain hardening region. Nonetheless, the effect of strain rate on yield strength of the samples is well understood. Figure 5.3 summarizes the significant conclusion of our analysis: Au thin films with sub-micron thickness exhibits strain-rate dependent yield behavior. There is an almost linear trend between the logarithm of the strain rate and the strength of the metal. This result has not been supported by further microstructural analyses, however it affirms that metals confined into small dimensions can have enhanced strength under higher-rate stimulus conditions.

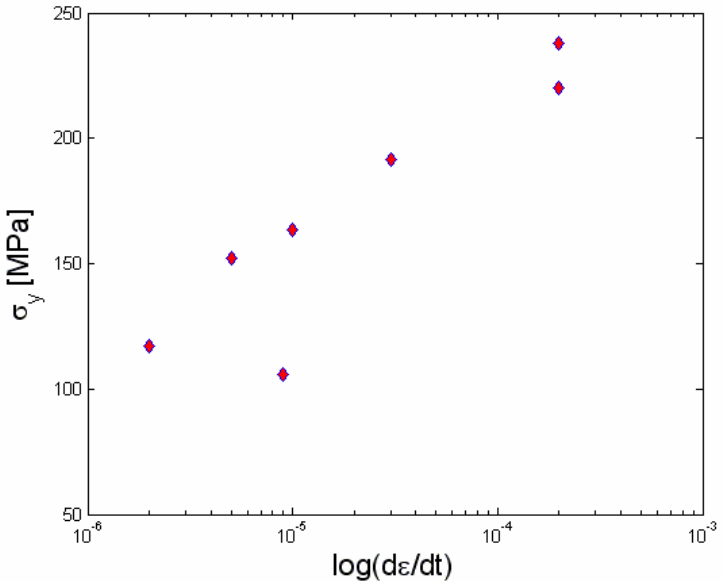

Figure 5.3: Strain Rate Dependent Yield Strength of Au

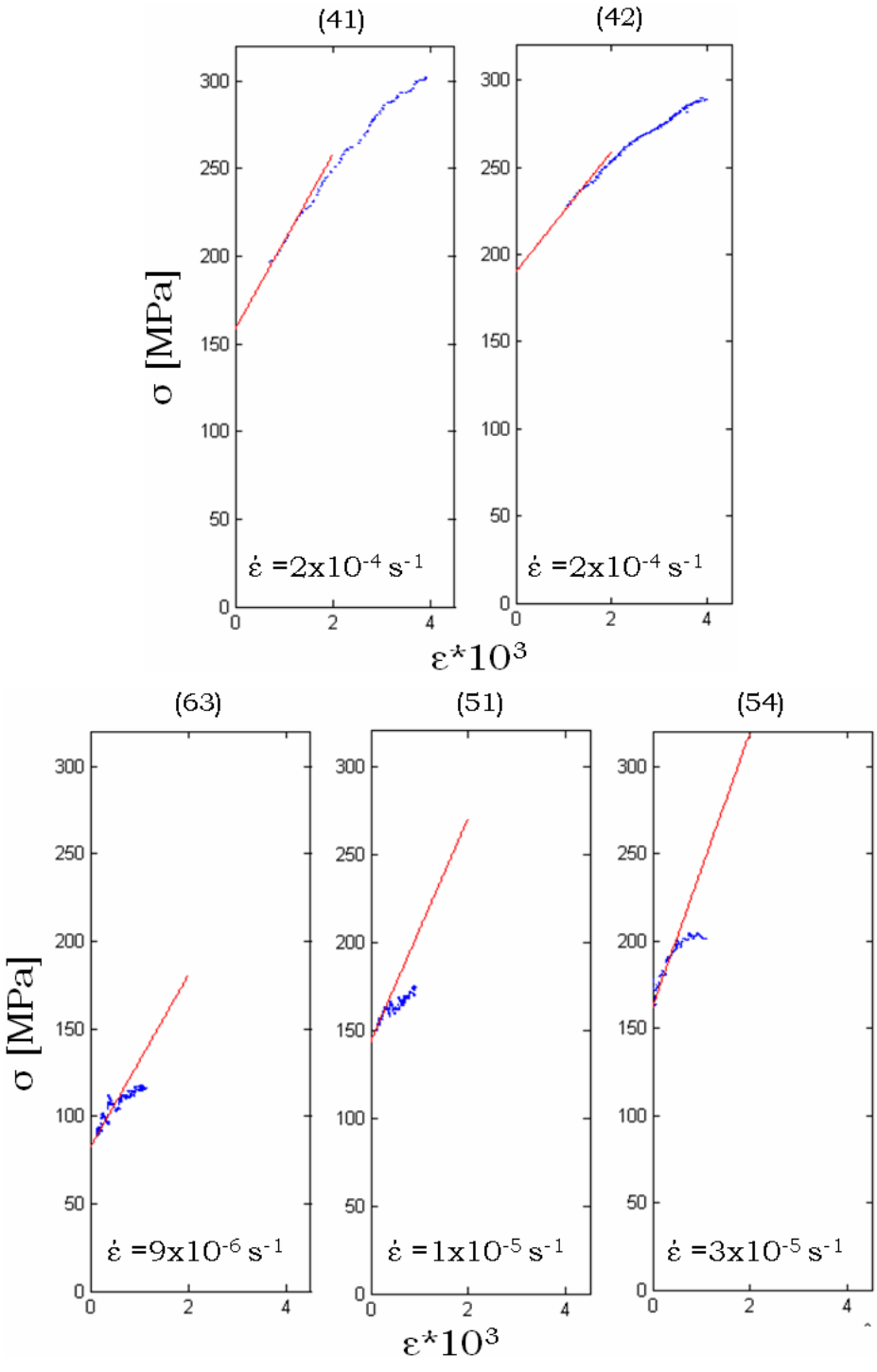
(41)
(42)
σ [MPa]
ε̇ =2x10-4 s-1
ε̇ =2x10-4 s-1
ε*10³
(63)
(51)
(54)
σ [MPa]
ε̇ =9x10-6 s-1
ε̇ =1x10-5 s-1
ε̇ =3x10-5 s-1
ε*10³

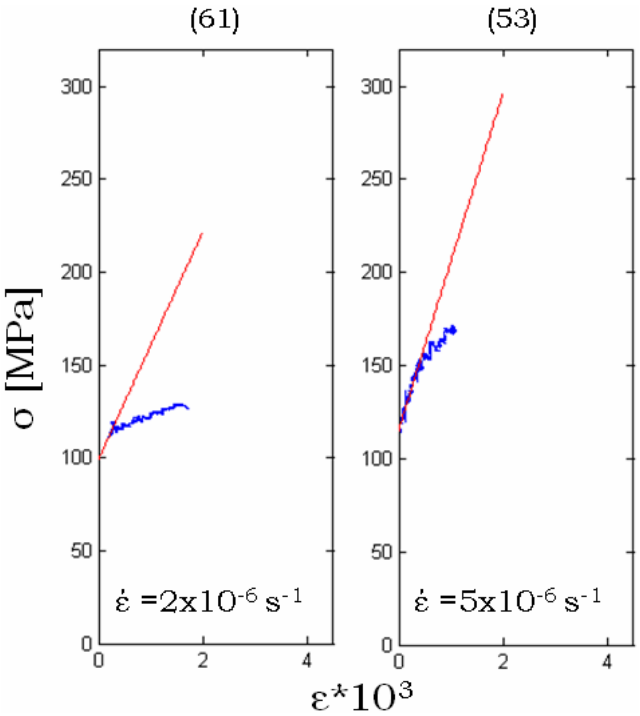

Figure 5.4: Stress-Strain Diagrams

Table 5.3 summarizes the results retrieved from the stress-strain diagrams. Yield stress is located at the inflection point of the stress-strain curve where transition from elastic region to plastic flow occurs. Despite the large fluctuations, yield points are easily detectable in the stress-strain diagrams. For the sake of easy perception, the experimental data in figures 5.4 are plotted with hypothetical red elastic lines.

Table 5.3: Summary of Results

#	a [μm]	E [GPa]	σ_Residual [MPa]	σ_Yield [MPa]	ε̇ [s^{-1}]
42	300	28.3	190.3	237.8	2.00E-04
41	310	40.8	158.5	220.3	2.00E-04
54	160	64.2	162.4	191.6	3.00E-05
51	240	52.0	143.6	163.5	1.00E-05
53	240	74.2	115.4	152.1	5.00E-06
61	180	50.2	99.2	117.2	2.00E-06
63	160	40.3	82.2	105.6	9.00E-06

The strength of the sputtered gold samples varies between 105.6 and 237.8 MPa for all strain rate measurements. These values are compatible with literature. Espinosa *et al.* observed approximately 220 MPa strength for 500 nm thick evaporated gold cantilevers yielded at 6 10^{-5} s^{-1} strain rate [43]. This result fits well to the linear trend that is presented in figure 5.3. The strength of evaporated gold samples presented by Chasiotis *et al*. [11], Wang *et al*. [42] and Emery *et al*. [40, 41] are 40-200 MPa higher than the ones in table 5.3. On the other hand, in Ref.12, sputtered nanocrystalline gold sample tested at 1 10^{-4} s^{-1} strain rate exhibited 70 MPa yield strength which overestimates our findings. The results we present for the sputtered gold is highly in corporation with the ones in literature.

5.4. Conclusion & Future Work

Bulge test has been proved to be capable of achieving various tasks in mechanical characterization of small structures so far. The literature related to this technique is still in extension. The scientific contribution of this project is on a bulge test affiliated issue that has been studied by other characterization techniques. The strain rate dependent mechanical behavior of sub-micron thickness gold membranes has been investigated. The previous studies on the same subject served a great opportunity to review the success of the current study. Both elasticity and plasticity results exhibits a consistent manner with the published research efforts. The overall performance of the technique on facilitating a solution to the strain rate control problem is satisfactory; however, there are two significant issues still demanding improvement. The resolution of the laser sensor is insufficient to study nano-scale bulging motion. The displacement sensor should be upgraded in order to achieve higher certainty in final results. The size of the diaphragms should be extended protecting the high aspect ratio of the rectangles. Thus, the amount of displacement attained by the motion of diaphragms shall increase healing the relative resolution of the measurements. The increment in the measurable displacement and the size of the diaphragms may decrease the maximum attainable

pressure. Such a trade-off decreases the odds to observe the complete mechanical behavior of diaphragms. Hence, the isolation of the closed fluid chamber becomes more critical. The size of the fluid chamber can be required to decrease as well. In addition to the design modifications, a thicker substrate can be desired to diminish the effect of substrate deflection. Although, the substrate deflection issue has been solved in this study, its vacancy will simplify the whole experimental procedure.

Appendix

MATLAB CODE: DATA FILTERING

```
clc
clear all
close all

A   = load('yielde-4.txt');
P   = A(:,1);
x1  = A(:,2);

R   = 0.01;
wn = 0.0015;

[a,b]= cheby1(2,R,wn);
xfe1 = filtfilt(a,b,x1);

plot(x1,p,'*')
hold on
plot(xfe1,p,'r')
xlabel('Deflection [Volt]')
ylabel('Pressure [Volt]')

p_min = min(p);
p = p-p_min;
fid = fopen('p.txt','wt');
fprintf(fid,'%4.3f\n',p);
fclose(fid);

d_min = min(xfe1);
xfe1 = xfe1-d_min;
fid = fopen('d.txt','wt');
fprintf(fid,'%7.6f\n',xfe1);
fclose(fid);
```

BIBLIOGRAPHY

[1] F. Spaepen, Interfaces and stresses in thin films, Acta Materialia, 48 (2000), 31-42.

[2] S. M. Spearing, Materials issues in microelectromechanical systems (MEMS), Acta Materialia, 48 (2000), 179-196.

[3] E. Arzt, Size effects in materials due to microstructural and dimensional constraints: A comparative review, Acta Materialia, 46 (1998), 5611-5626.

[4] W. D. Nix, Mechanical properties of thin-films. Metallurgical Transactions A, 20A (1989), 2217-2245.

[5] V. T. Srikar, S. M. Spearing, A critical review of microscale mechanical testing methods used in the design of microelectromechanical systems. Experimental Mechanics, 43 (2003), 238-247.

[6] O. Kraft, C. A. Volkert, Mechanical testing of films and small structures, Advanced Engineering Materials, 3 (2001), 99-110.

[7] W. C. Oliver, G. M. Pharr, Measurement of hardness and elastic modulus by instrumented indentation: Advances in understanding and refinements to methodology, J. Materials Research, 19 (2004), 3-20.

[8] J. B. Pethica, R. Hutchings, W. C. Oliver, Hardness measurement at penetration depths as small as 20 nm, Phil. Mag. A, 48 (1983), 593-606.

[9] E. Martinez, J. Romeo, A. Lousa, J. Esteve, Nanoindentation stress-strain curves as a method for thin film complete mechanical characterization: Application to nanometric CrN/Cr multilayer coatings, Applied Physics A, 77 (2003), 419-426.

[10] G. G. Stoney, The tension of metallic films deposited by electrolysis, Proc. R. Soc. London A, 82 (1909), 172

[11] I. Chasiotis, C. Bateson, K. Timpano, A. S. McCarty, N. S. Barker, J. R. Stanec, Strain rate effects on the mechanical behavior of nanocrystalline Au films, Thin Solid Films, 515 (2007), 3183-3189.

[12] J. Rajagopalan, J. H. Han, M. T. A. Saif, Plastic deformation recovery in freestanding nanocrystalline aluminum and gold thin films, Science, 315 (2007) 1831-1834.

[13] M. A. Haque, M. T. A. Saif, In situ tensile testing of nanoscale freestanding thin films inside a transmission electron microscope, J. Materials Research, 20 (2005), 1769-1777.

[14] J. W. Beams, Mechanical properties of thin films of gold and silver, in Structure and Properties of Thin Films, edited by C.A. Neugebauer, J.B. Newkirk, and D.A. Vermilyea (John Wiley and Sons, New York, 1959), p. 183.

[15] J. J. Vlassak, W. D. Nix, A new bulge test technique for the determination of Young's modulus and Poisson's ratio of thin films, J. Materials Research, 7 (1992) 3242-3249.

[16] M. K. Tripp, C. Stampfer, D. C. Miller, T. Helbling, C. F. Herrmann, C. Hierold, K. Gall, S. M. George, V. M. Bright, The mechanical properties of atomic layer deposited alumina for use in micro- and nano-electromechanical systems, Sensors and Actuators A, 130-131 (2006), 419-429.

[17] O. R. Shojaei, A. Karimi, Comparison of mechanical properties of TiN thin films using nanoindentation and bulge test, Thin Solid Films, 332 (1998), 202-208.

[18] R. L. Edwards, G. Coles, W. N. Sharpe, Jr, Comparison of tensile and bulge tests for thin-film silicon nitride, Experimental Mechanics, 44 (2004), 49-54.

[19] M. A. Haque, M. T. A. Saif, A review of MEMS-based microscale and nanoscale tensile and bending testing, Experimental Mechanics, 43 (2003) 248-255.

[20] C. K. Huang, W. M. Lou, C. J. Tsai, T. Wu, H. Lin, Mechanical properties of polymer thin film measured by the bulge test, Thin Solid Films, 515 (2007), 7222-7226.

[21] J. S. Mitchell, C. A. Zorman, T. Kicher, S. Roy, M. Mehregany, Examination of bulge test for determining residual stress, Young's modulus and Poisson's ratio of 3C-SiC thin films, J. Aerospace Engineering, 16 (2003), 46-54.

[22] E. I. Bromley, J. N. Randall, D. C. Flanders, R. W. Mountain, A technique for the determination of stress in thin films, Journal of Vacuum Science & Technology B: Microelectronics and Nanometer Structures, B1(4) (1983), 1364-1366.

[23] A. J. Kalkman, A. H. Verbruggen, G. C. A. M. Janssen, Young's modulus measurements and grain boundary sliding in free-standing thin metal films, Applied Physics Letters, 78 (2001), 2673-2675.

[24] J. D. Hall, N. E. Apperson, B. T. Crozier, C. Xu, R. F. Richards, D. F. Bahr, C. D. Richards, A facility for characterizing the dynamic mechanical behavior of thin membranes for microelectromechanical systems, Review of Scientific Instruments, 73(5) (2002), 2067-2072.

[25] B. E. Alaca, J. C. Selby, M. T. A. Saif, and H. Sehitoglu, Biaxial testing of nano-scale films on compliant substrates – fatigue and fracture, Review of Scientific Instruments 73(8), (2002), 2963-2970.

[26] A. J. Kalkman, A. H. Verbruggen, G. C. A. M. Janssen, S. Radelaar, Transient creep in free-standing thin polycrystalline aluminum films, J. Applied Physics, 92 (2002), 4968-4975.

[27] A. J. Kalkman, A. H. Verbruggen, G. C. A. M. Janssen, High-temperature bulge-test setup for mechanical testing of free-standing thin films, Review of Scientific Instruments, 74 (2003), 1383-1385.

[28] M. Cieslar, V. Oliva, A. Karimi, J.-L. Martin, The influence of temperature on plastic deformation of free standing thin Al–Zn–Mg–Cu films, Journal of Alloys and Compounds, 378 (2004), 312–315.

[29] S. Hyun, T. K. Hooghan, W. L. Brown, R. P. Vinci, Linear viscoelasticity in aluminum thin films, Applied Physics Letters, 87 (2005), 061902 1-3.

[30] X. Wei, D. Lee, S. Shim, X. Chena, J. W. Kysar, Plane-strain bulge test for nanocrystalline copper thin films, Scripta Materialia, 57 (2007), 541–544.

[31] Y. Xiang, X. Chen, J. J. Vlassak, The plane-strain bulge test for thin films, J. Materials Research 20(9) (2005), 2360-2370.

[32] Y. Xiang, T.Y. Tsui, J. J. Vlassak, The mechanical properties of freestanding electroplated Cu thin films, J. Materials Resesearch, 21(6) (2006), 1607-1618.

[33] J. S. Mitchell, C. A. Zorman, T. Kicher, S. Roy, M. Mehregany, Examination of bulge test for determining residual stress, Young's Modulus, and Poisson's ratio of 3C-SiC thin films, Journal of Aerospace Engineering, 16(2) (2003), 46-54.

[34] X. Fu, J. L. Dunning, C. A. Zorman, M. Mehregany, Measurement of residual stress and elastic modulus of polycrystalline 3C-SiC films deposited by low-pressure chemical vapor deposition, Thin Solid Films, 492 (2005), 195–202.

[35] A. Kaushik, H. Kahn, A. H. Heuer, Wafer-level mechanical characterization of Silicon Nitride MEMS, Journal of Microelectromechanical Systems, 14(2) (2005), 359-367.

[36] D. W. Zheng, Y. H. Xu, Y. P. Tsai, K. N. Tu, C. P. Patterson, B. Zhao, Q.-Z. Liu, M. Brongo, Mechanical property measurement of thin polymeric-low dielectric-constant films using bulge testing method, Applied Physics Letters, 76(15) (2000), 2008-2010.

[37] Y. Xu, Y. Tsai, D. W. Zheng, K. N. Tu, C. W. Ong, C. L. Choy, B. Zhao, Q.-Z. Liu, M. Brongo, Measurement of mechanical properties for dense and porous polymer films having a low dielectric constant, Journal of Applied Physics, 88(10) (2000), 5744-5750.

[38] C. K. Huang, W. M. Lou, C. J. Tsai, T. -C. Wu, H. -Y. Lin, Mechanical properties of polymer thin film measured by the bulge test, Thin Solid Films, 515(18) (2007), 7222-7226.

[39] LMI Selcom - SLS 7000 Device Manual (2002)

[40] R. D. Emery, G. L. Povirk, Tensile behavior of free-standing gold films. Part I. Coarse-grained films, Acta Materialia, 51 (2003), 2067-2078.

[41] R. D. Emery, G. L. Povirk, Tensile behavior of free-standing gold films. Part II. Fine-grained films, Acta Materialia, 51 (2003), 2079-2087.

[42] L. Wang, B. C. Prorok, Characterization of the strain rate dependent behavior of nanocrystalline gold films, J. Matereials Research, 23(1) (2008), 55-65.

[43] H. D. Espinoza, B. C. Prorok, B. Peng, Plasticity size effects in free-standing submicron polycrystalline FCC films subjected to pure tension, J. the Mechanics and Physics of Solids, 52 (2004), 667-689.

[44] T. H. Courtney, Poisson's ratio of metals, in Mechanical behavior of materials (McGraw-Hill, Inc. TA405.C859, 1990), p.59-60

[45] W. L. Winterbottom, N. A. Gjostein, Determination of the anisotropy of surface energy of metals—II: Experimental γ-plot of gold, Acta metallurgica et Materialia, 14(9) (1966), 1041-1052.